

# Random Wave-Induced Seabed Responses around Breakwater Heads

Y Zhang<sup>1</sup>, D-S Jeng<sup>1,2</sup>, Z-W Fu<sup>3</sup> and J Ou<sup>4</sup>

<sup>1</sup>Centre for Marine Geotechnical Engineering, Shanghai Jiao Tong University, Shanghai 200240, China

<sup>2</sup>Griffith School of Engineering, Griffith University Gold Coast Campus, QLD 4111, Australia

<sup>3</sup>Wessex Institute of Technology, Southampton, UK

<sup>4</sup>University of Birmingham, Birmingham, UK

E-mail: jengd2@asme.org

**ABSTRACT:** Wave-induced pore pressures and effective stresses in a porous seabed around breakwater heads have been recognised as one of the key factors in the design of breakwaters. Unlike previous investigations, which were limited to regular wave loading, this paper investigated random wave-induced seabed responses. Two common wave spectra, B-M and JONSWAP, were used for the simulation of random waves in a model. Based on this poro-elastoplastic model, the influence of random wave parameters, waves and seabed parameters on the pore pressures around breakwater heads were examined and discussed in detail.

## 1. INTRODUCTION

Breakwaters are commonly constructed to reduce or eliminate the detrimental effects of wave forces on beaches, bluffs, dunes or harbour regions. When waves approach, the accompanying wave energy drives sediments to drift along the coast, resulting in erosion. The installation of breakwaters is an effective way to reduce erosion by forming an area of slack water behind the breakwater. Deposition occurs in this area and the beach is built up. On the other hand, the areas in front of the structure tend to shrink. In practice, breakwaters are seldom built for mere maintenance of a coastline's natural features, but are more often built for engineering purposes due to the high investment costs and possible renovation needs.

When waves propagate towards breakwater heads, the incident waves are reflected, diffracted and then combined. As illustrated in Figure 1, the region in the vicinity of a breakwater can generally be divided into four zones (Stoker, 1957). First, the incident wave components in Zone A interact with their reflected wave components, forming a short-crested wave system along the breakwater. Next, the diffraction effects in Zone B can be detected along with incident and reflected waves due to the discontinuity of the marine structure. Third, because there is no reflected wave component, Zone C contains the combined effect of incident and diffracted waves. Finally, there are only diffracted wave components in Zone D, which lie behind the breakwater.

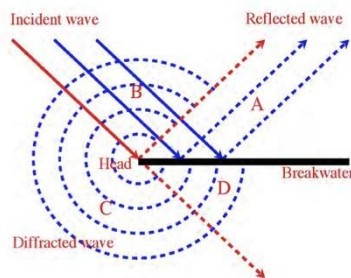


Figure 1 Definition of the wave-seabed interaction around breakwater heads

The interaction of the above three wave components complicates the soil response around breakwater heads. In particular, the components of wave diffraction affect the distribution of wave-induced pore pressure (Li and Jeng, 2008). In the past, damage has been observed in numerous marine structures due to seabed instability at the tips of these structures (Smith and Gordon, 1983). In Deep scours have also been reported at the toes of marine structures (Gökee et al., 1994; Sumer and Fredsøe, 2002).

Numerous investigations on wave-induced seabed responses have been carried out since the 1980s. Most of these studies have focused on 2D cases (Yamamoto et al., 1978; Mei and Foda, 1981; Okusa, 1985), while the first author and his co-workers (Jeng and Hsu, 1996; Jeng, 2013) have, for the first time, investigated the 3D short crested wave-induced soil response in a porous seabed. In addition to wave and soil parameters, a new parameter has also been introduced that indicates a complex relationship between the wave's obliquity and soil parameters. However, almost all of these studies have concentrated on wave-induced soil responses in front of a vertical wall, not around breakwater heads. To date, only a few publications on the wave-induced seabed responses around breakwater heads have been found in the literature (Jeng, 1996; Sassa et al., 2006; Li and Jeng, 2008; Jeng and Ou, 2010). Among these, Jeng (1996) has proposed an analytical solution for the wave-induced liquefaction potential at the tip of a breakwater and demonstrated the significant contributions from diffracted waves. However, a mistake in Jeng (1996) has been identified by Li and Jeng (2008), leading to the creation of a new 3D model that uses the finite difference method after the correction of the mistake. In addition to the oscillatory mechanism, the wave-induced residual liquefaction has also been considered in Li and Jeng (2008). A parametric study has revealed that the wave angle directly affects the magnitude and distribution of wave-induced liquefaction around breakwater heads, and two residual parameters  $\lambda$  and  $\delta$  have been analysed and proved to be related to the equilibrium pore pressure. A 3D poro-elastoplastic model has been further developed by the first author to examine its liquefaction potential (Jeng and Ou, 2010). These investigations have considered only regular wave loading, although random waves have also been observed in real ocean environments (Goda, 2000). In addition to theoretical studies, Sassa et al. (2006) conducted a series of field observations and numerical simulations for the seabed response around breakwater heads. The numerical model he used was based on his previous model (Sassa and Sekiguchi, 2001) that considered the rotation of principal stress axis induced in the seabed soil.

Regarding random wave-induced soil response, Liu and Jeng (2007) presented a semi-analytical solution for random wave-induced soil response in marine sediments. Later, Xu and Dong (2011) further investigate the random nature of waves, namely randomness of wave height, through a numerical study.

In this paper, the previous poro-elastoplastic model for the wave-induced seabed response around breakwater heads (Jeng and Ou, 2010) was further developed by including random wave loading. The random wave model and poro-elastoplastic seabed model are outlined here first. Based on the numerical model, the convergence of the finite element model and verification against the previous model (Jeng and Ou, 2010) is presented. Next, a detailed parametric study is described that examines the effects of both wave and seabed characteristics on the seabed responses around breakwater heads.

## 2. THEORETICAL FORMULATIONS

### 2.1 Random waves around breakwater heads

In realistic oceanic environments, waves approaching breakwaters are random rather than regular. To analyse the wave conditions around a breakwater head, a circular domain was applied with the central point at the toe of the breakwater (seen Figure 2a). By establishing a polar coordinate system, the incident wave angle ( $\alpha$ ) was defined as the angle between the incident wave and the breakwater. The radius  $r$  represented the distance from the circular centre point to a studied point in the domain.

Such waves, characterised by random surface water elevations, bring about corresponding dynamic pressure, which is situated on the surface of the seabed. As shown in a 2D view along the propagating direction (Figure 2b),  $d$  is the water depth from the still water level (SWL) to the seabed surface and  $h$  is the thickness of the porous seabed.

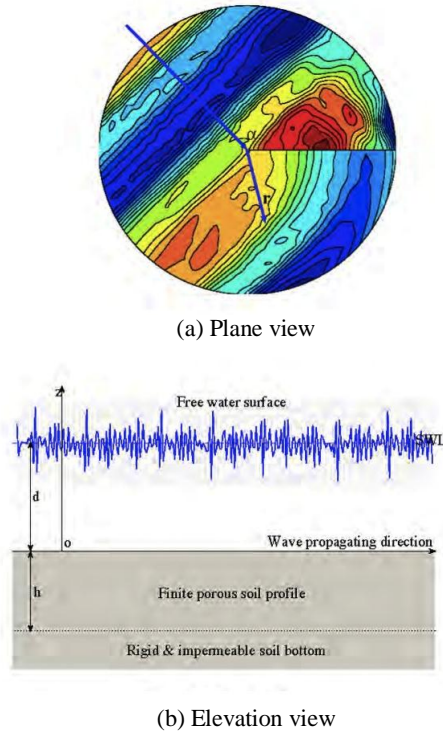


Figure 2 Sketch of random waves propagating towards a breakwater head with wave obliquity ( $\alpha$ )

#### 2.1.1 Wave theory around breakwater heads

First, we considered a series of monochromatic waves that propagate towards a vertical breakwater. The wave parameters are prescribed with a specific wave height  $H$  and wave period  $T$ . The analytical solution for the velocity potential ( $\phi$ ) and the water surface elevation ( $\eta$ ) can be obtained as:

$$\phi = \text{Re} \left\{ -\frac{igH_i}{2\omega} \frac{\cosh kz}{\cosh kd} \sum_{m=0}^{\infty} e^{-i\omega t} e^{-im\pi/4} \varepsilon_m \mathfrak{J}_{m/2}(kr) \cos \frac{m\alpha}{2} \cos \frac{m\theta}{2} \right\} \quad (1)$$

$$\eta = \text{Re} \left\{ \frac{H_i}{2} \sum_{m=0}^{\infty} e^{-i\omega t} e^{-im\pi/4} \varepsilon_m \mathfrak{J}_{m/2}(kr) \cos \frac{m\alpha}{2} \cos \frac{m\theta}{2} \right\} \quad (2)$$

$$\varepsilon_m = \begin{cases} 1 & m = 0 \\ 2 & m \neq 0 \end{cases} \quad (3)$$

where  $\mathfrak{J}_{m/2}$  is the first type of Bessel Function of order  $m/2$ ,  $H_i$  is the incident wave height and  $k$  is the wave number. Meanwhile, the

wave angular frequency  $\omega$  and  $k$  satisfy the linear wave dispersion relationship:

$$\omega^2 = gk \tanh kd \quad (4)$$

Based on (1) and (2), the dynamic pressure on the seabed surface is obtained as:

$$P_{d,avg} = \text{Re} \left\{ p_0 \sum_{m=0}^{\infty} e^{-i\omega t} e^{-im\pi/4} \varepsilon_m \mathfrak{J}_{m/2}(kr) \cos \frac{m\alpha}{2} \cos \frac{m\theta}{2} \right\} \quad (5)$$

where

$$p_0 = \frac{\gamma_w H_i}{2 \cosh kd} \quad (6)$$

Note that we consider only the wave interactions around the breakwater heads. In fact, currents are likely to co-exist with the waves in marine environments. For the influence of currents on the seabed response, the reader can refer to the work of Ye and Jeng (2011), although this study has used a 2D model to investigate wave-seabed interactions.

#### 2.1.2 Wave theory around breakwater heads

The concept of a frequency spectrum was introduced to study the profiles of random waves. Sea waves, which seem very random, can actually be analysed by considering the fact that they consist of an infinite number of wavelets with various frequencies and directions (Goda, 2000). The wave spectrum is obtained mainly based on records in a particular area of water, and the characteristics of wave spectra vary with different water conditions. Two typical spectra are commonly adopted for random wave analysis in engineering practice.

##### (1) B-M Spectrum

In general, the B-M spectrum agrees quite well with the actual spectrum in which wind is fully developed for wave generation. The formula is expressed as (Goda, 2000):

$$S(f) = 0.257 H_{1/3}^2 T_{1/3}^{-4} f^{-5} \exp(-1.03(T_{1/3} f)^4) \quad (7)$$

where  $H_{1/3}$  and  $T_{1/3}$  denote the one-third representative wave height and corresponding representative wave period, respectively.

##### (2) JONSWAP Spectrum

The JONSWAP Spectrum is based on data from the North Sea and can be described in an approximate form as (Goda, 2000):

$$S(f) = \beta_j H_{1/3}^2 T_p^{-4} f^{-5} \exp(-1.25(T_p f)^4) \gamma^{\exp(-(T_p f - 1)/2\sigma^2)} \quad (8)$$

in which

$$\beta_j = \frac{0.0624(1.094 - 0.01915 \ln \gamma)}{0.23 + 0.0336\gamma - 0.185(1.9 + \gamma)^{-1}} \quad (9a)$$

$$T_p \approx \frac{T_{1/3}}{1 - 0.132(0.2 + \gamma)^{-0.559}} \quad (9b)$$

$$\sigma = \begin{cases} \sigma_a \approx 0.07: & f \leq f_p \\ \sigma_b \approx 0.09: & f \geq f_p \end{cases} \quad (9c)$$

where  $\gamma$  represents the peak enhancement factor ( $=1\sim7$ ), which has a mean value of 3.3 for the North Sea, and  $T_p$  denotes the wave period corresponding to the frequency  $f_p$  at the spectrum peak.

The random wave profile can be expressed using various mathematical methods, such as a method using linear superposition. Based on (2) and the assumption that random waves are composed of an infinite number of wavelets, the surface water elevations of random waves around breakwater heads can be expressed as:

$$\eta(r, \theta, \alpha, t) = \text{Re} \left\{ \sum_{n=1}^{\infty} \frac{H_n}{2} \sum_{m=0}^{\infty} e^{-i\omega_n t} e^{-im\pi/4} \varepsilon_m \mathfrak{S}_{m/2}(k_n r) \cos \frac{m\alpha}{2} \cos \frac{m\theta}{2} \right\}$$

$$\approx \text{Re} \left\{ \sum_{n=1}^{M_r} \frac{H_n}{2} \sum_{m=0}^{M_b} e^{-i\omega_n t} e^{-im\pi/4} \varepsilon_m \mathfrak{S}_{m/2}(k_n r) \cos \frac{m\alpha}{2} \cos \frac{m\theta}{2} \right\} \quad (10)$$

where  $M_b$  is the number of Bessel Function terms and  $M_r$  is the number of wave components with unique frequencies. It is assumed that  $M_b$  is large enough for any wavelet of random waves to reach a stable state (e.g., water elevation  $\eta$  and dynamic pressure  $P_b$ ). The larger the number of wave components, the more accurate the adopted formula is at simulating realistic wave conditions. A detailed discussion on  $M_b$  and  $M_r$  is provided in a later section. The wave height  $H_n$  of the relevant wavelet has a value related to the frequency and spectrum:

$$H_n = \sqrt{s(\tilde{f}_n) D f_n / 2} \quad (11)$$

Similarly, the random wave-induced dynamic pressure on a seabed surface can also be expressed as:

$$P_d = \text{Re} \left\{ \sum_{n=1}^{\infty} P_{0n} \sum_{m=0}^{\infty} e^{-i\omega_n t} e^{-im\pi/4} \varepsilon_m \mathfrak{S}_{m/2}(k_n r) \cos \frac{m\alpha}{2} \cos \frac{m\theta}{2} \right\}$$

$$\approx \text{Re} \left\{ \sum_{n=1}^{M_r} P_{0n} \sum_{m=0}^{M_b} e^{-i\omega_n t} e^{-im\pi/4} \varepsilon_m \mathfrak{S}_{m/2}(k_n r) \cos \frac{m\alpha}{2} \cos \frac{m\theta}{2} \right\} \quad (12)$$

where

$$P_{0n} = \frac{\gamma_w H_n}{2 \cosh k_n d} \quad (13)$$

## 2.2 Poro-elastoplastic seabed model

### 2.2.1 u-p model

A three-dimensional poro-elasto-plastic model for the interaction between soil and a pore fluid was developed based on the fully implicit u-p approximation of the Biot formulation (Biot, 1956a; 1956b; Zienkiewicz et al., 1999). The dynamic governing equations for the u-p approximation of the Biot formulation are essentially the momentum equations for the soil-fluid “mixture” and the mass balance of the flow. We provide only a brief outline of the theory in this section. Further details can be found in (Zienkiewicz et al., 1999).

(i) The conservation of mass for fluid phase is expressed as:

$$w_{,i} + \alpha \frac{\partial \varepsilon_{ii}}{\partial t} + \frac{1}{Q} \frac{\partial p}{\partial t} = 0 \quad (14)$$

$$\partial = \left( 1 - \frac{K_r}{K_s} \right), \quad \frac{1}{Q} = \frac{n}{K_f} + \frac{(1-n)}{K_s} \quad (15)$$

where  $u$  denotes the soil displacements,  $w$  represents the relative displacement of the pore fluid to the solid particles,  $K_r$  is the average bulk modulus of the solid skeleton,  $K_s$  is the average material bulk modulus of the solid components of the skeleton,

$K_f$  is the bulk modulus of the fluid,  $w_{,ii}$  is the flow divergence in the unit volume,  $\varepsilon_{ii}$  is the increased volume due to a change in strain, and  $np/K_f$  is the additional volume stored by the compression of void fluid due to the fluid pressure increase.

(ii) The equilibrium of the mixture can be expressed as:

$$\sigma_{ij,j} + \rho b_i - \rho \frac{\partial^2 u_i}{\partial t^2} - \rho_f \frac{\partial w_i}{\partial t} = 0 \quad (16)$$

where  $\sigma_{ij}$  is the total stress tensor (tensile positive),  $u_i$  is the displacement of the solid skeleton,  $w_i$  is the average (Darcy) fluid velocity,  $b_i$  is the body force per unit mass and  $\rho_s$ ,  $\rho_f$  and  $\rho$  are the densities of the solid grain, fluid and mixture, respectively, in which  $\rho = (1-n)\rho_s + n\rho_f$  and  $n$  is the porosity of the porous medium.

(iii) The equilibrium of the fluid can be expressed as:

$$-p_{,i} - R_i - \rho_f \frac{\partial^2 u_i}{\partial t^2} - \rho_f b_i - \frac{\rho_f}{n} \frac{\partial w_i}{\partial t} = 0 \quad (17)$$

where  $R_i$  represents the viscous drag forces, which, assuming the Darcy seepage law, can be written as  $w_i = k_{ij} R_j / (\rho' g')$ , and  $k_{ij}$  is the permeability tensor of soil using the dimensions of [length]/[time] (for isotropic permeability,  $k_{ij} = k \delta_{ij}$ ,  $\delta_{ij}$  is the Kronecker delta), where  $\rho'$  and  $g'$  are the fluid density and gravitational acceleration at which the permeability is measured, respectively.

Using (14), (16) and (17), the governing equations can be expressed as:

$$\sigma_{ij,j} + \rho b_i - \rho \frac{\partial^2 u_i}{\partial t^2} = 0 \quad (18)$$

$$(k_{ij} (-p_{,j} - \rho_f \frac{\partial^2 u_j}{\partial t^2} + \rho_f b_j))_{,i} + \alpha \varepsilon_{ii} + \frac{1}{Q} \frac{\partial p}{\partial t} = 0 \quad (19)$$

Because this simplified equation set, consisting of (18) and (19), contains only two independent variables,  $u$  and  $p$ , it is usually called the  $u$ - $p$  approximation.

### 2.2.2 Soil constitutive models

The generalised plastic model proposed by Zienkiewicz et al. (1989) was used to describe plastic soil behaviour under wave loading. We outline the model in the following paragraphs.

Let  $p^{\ell}$  and  $q^{\ell}$  denote the mean effective stress and deviatoric stress, respectively, which can be expressed as:

$$p^{\ell} = \frac{1}{3} (S_{f1}^{\ell} + S_{f2}^{\ell} + S_{f3}^{\ell}) \quad (20)$$

$$q^{\ell} = \left\{ \frac{2}{3} (S_{f1}^{\ell} - S_{f2}^{\ell})^2 + (S_{f1}^{\ell} - S_{f3}^{\ell})^2 + (S_{f2}^{\ell} - S_{f3}^{\ell})^2 + 6 (S_{f2}^{\ell 2} + S_{f3}^{\ell 2} + S_{f31}^{\ell 2}) / 3 \right\}^{1/2} \quad (21)$$

In the generalised plastic model, it is suggested that the strain increment be decomposed into two parts:

$$\dot{e}_{ij} = \dot{e}_{ij}^e + \dot{e}_{ij}^p \quad (22)$$

where  $e_{ij}^e$  is the elastic strain-rate tensor and  $e_{ij}^p$  is the plastic strain-

rate tensor. The elastic strain tensor  $\dot{S}_{ij}$  is related to the effective stress-rate tensor through Hooke's law of elasticity. If the volumetric and deviatoric strains are considered separately, it can be written as:

$$\dot{e}_v^e = \frac{p^c}{K_{ev}} \text{ and } \dot{e}_s^e = \frac{q^c}{G_{es}} \quad (23)$$

where  $e_v^e$  is the volumetric strain,  $e_s^e$  is the deviatoric strain,  $K_{ev}$  is the soil bulk modulus and  $G_{es}$  is the shear modulus. However, it should be noted that the elastic constants depend on the mean effective stress ( $p^c$ ) in this plastic model and can be expressed as:

$$K_{ev} = K_{ev0} \frac{p^c}{p_0^c} \text{ and } G_{es} = G_{eso} \frac{p^c}{p_0^c} \quad (24)$$

The plastic strain-rate tensor ( $\dot{e}_{ij}^p$ ) is most conveniently described using three scalar functions (Zienkiewicz et al., 1989): the loading function  $f(p^c, q^c)$ , plastic function  $g(p^c, q^c)$  and plastic modulus at the loading/unloading stage  $H_{L/U}(p^c, q^c, \chi)$ . The parameter here represents the accumulated plastic strain defined by:

$$\chi = \int_0^t \sqrt{\dot{e}_{ij}^p \dot{e}_{ij}^p} dt \quad (25)$$

The loading function ( $f$ ) and the plastic flow function ( $g$ ) are given in the model as:

$$f = q^c - M_{f0} p^c \left[ 1 + \frac{1}{a_0} \frac{\dot{e}_v^e}{\dot{e}} \right] + \frac{p^c}{p_f} \left[ 1 + \frac{\dot{e}_v^e}{\dot{e}} \right] = 0 \quad (26)$$

$$g = q^c - M_{g0} p^c \left[ 1 + \frac{1}{a_0} \frac{\dot{e}_v^e}{\dot{e}} \right] + \frac{p^c}{p_g} \left[ 1 + \frac{\dot{e}_v^e}{\dot{e}} \right] = 0 \quad (27)$$

in which  $p_f$  and  $p_g$  are constants characterising the size of both surfaces and  $a_0$  is a coefficient related to the stress-dilatancy relationship of the soil.  $M_{g0}$  represents the slope of the phase transformation line and  $M_{f0}$  is a material parameter given by:

$$\frac{M_{f0}}{M_{g0}} = D_r \quad (28)$$

where  $D_r$  is the elastic density of the soil.

Using the definitions of the plastic flow function ( $g$ ) and loading function ( $f$ ), the plastic flow direction ( $m_{ij}$ ) and loading-unloading direction ( $n_{ij}$ ) can be defined as:

$$m_{ij} = \frac{\frac{\partial g}{\partial S_{ij}}}{\left\| \frac{\partial g}{\partial S_{ij}} \right\|} \text{ and } n_{ij} = \frac{\frac{\partial f}{\partial S_{ij}}}{\left\| \frac{\partial f}{\partial S_{ij}} \right\|} \quad (29)$$

where  $\left\| \frac{\partial g}{\partial S_{ij}} \right\|$  and  $\left\| \frac{\partial f}{\partial S_{ij}} \right\|$  represent the norms of the tensors  $\frac{\partial g}{\partial S_{ij}}$  and  $\frac{\partial f}{\partial S_{ij}}$ , respectively. If the same function is adopted for both  $f$  and  $g$ , the associated flow rule can be applied; otherwise, the non-associated flow rule is applied.

Assuming a stress increment of  $dS$  and  $n$  is corresponding vector of the tensor, the loading criteria can then be expressed as:

$$\begin{aligned} n \times dS &> 0 \text{ for loading} \\ n \times dS &= 0 \text{ for neutral-loading} \\ n \times dS &< 0 \text{ for unloading} \end{aligned} \quad (30)$$

It should be noted that the aforementioned definition of the plastic flow vector has been proposed by Pastor et al. (1990) as the PZ3 model. It has been suggested by Chan (1989) that the following parameters be defined to make the constitutive model more suitable for a three-dimensional situation:

$$\begin{aligned} m_p &= (1 + a)(M_g - h), \quad m_q = 1, \\ m_q &= -qM_g \cos \frac{3q}{2} \text{ and } M_g = \frac{6 \sin f}{3 - \sin f \sin 3q} \end{aligned} \quad (31)$$

where  $q$  is the lode angle and  $f$  is the residual friction angle of the sand measured in a triaxial compression test when  $q = p/6$ .

Using the aforementioned definitions, the plastic strain-rate tensor ( $\dot{e}_{ij}^p$ ) can be expressed as:

$$\dot{e}_{ij}^p = \frac{n_{kl} \dot{S}_{kl}^c}{H_{L/U}} m_{ij} \quad (32)$$

$$H_L = H_0 p^c \left[ 1 - \frac{q^c/p^c}{h_f} \right] \left[ 1 - \frac{q^c/p^c}{h_{max}} \right]^{-g_{DM}} \frac{\dot{e}_v^e}{\dot{e}} - \frac{q^c/p^c}{M_{g0}} + b_0 b_1 e^{-b_0 \chi} \quad (33)$$

$$H_U = \begin{cases} H_{u0} \frac{M_{g0}}{h_u} \frac{\dot{g}_U}{\dot{e}} & \text{for } \left| \frac{M_{g0}}{h_u} \right| > 1 \\ H_{u0} & \text{for } \left| \frac{M_{g0}}{h_u} \right| \leq 1 \end{cases} \quad (34)$$

where  $h_u$  is the stress ratio at which the unloading takes place, while  $g_U$  is the material constant controlling the influence of  $i$  in (33) and (34),  $H_L$  and  $H_U$  are the plastic modulus during the loading and unloading stages, respectively, and  $H_0$  and  $H_{U0}$  are model parameters that scale the plastic modulus, while the dependency on  $p^c$  in (33) is consistent with the fact that the plastic strain decreases when the effective mean stress increases. The term  $\left[ 1 - \frac{q^c/p^c}{h_f} \right] \frac{\dot{e}_v^e}{\dot{e}}$  illustrates the fact that the plastic strain increment increases as the stress ratio increases, and the stress ratio cannot exceed  $h_f$ , where  $h_f = M_f(1 + 1/S_0)$ .

Using the appropriate definitions of  $m_{ij}$ ,  $n_{ij}$  and  $H_{L/U}$ , the constitutive relationships can be expressed as:

$$\dot{e}_{ij} = C_{ijkl}^e \dot{S}_{kl}^e + \frac{n_{kl} \dot{S}_{kl}^c}{H_{L/U}} m_{ij} \quad (35)$$

or its inverted form:

$$S_{ij}^c = \frac{\partial D_{ijkl}^e}{\partial C_{ijkl}^e} - \frac{D_{ijml}^e m_{mn} n_{st} D_{stkl}^e}{H_{L/U} + n_{st} D_{stkl}^e m_{kl}} \frac{\dot{e}_{kl}}{\dot{e}} \quad (36)$$

where  $C_{ijkl}^e$  and  $D_{ijkl}^e$  are the elastic compliance tensor and stiffness tensor, respectively.

During elastic behaviour, the stress–strain relationship, based on poro-elastic theory, can be expressed as:

$$\frac{\partial \sigma_{ij}}{\partial t} = D_{ijkl}^e \frac{\partial \varepsilon_{kl}^e}{\partial t} \quad (37)$$

where  $D_e$  represents the elements of the constitutive matrix that describes the constitutive stress–strain relationship, which can be expressed as follows for the case of isotropic elasticity:

$$D_{ijkl}^e = \lambda \delta_{ij} \delta_{kl} = 2G \delta_{ik} \delta_{jl} \quad (38)$$

where  $\lambda$  is Lamé’s constant and  $G$  is the shear modulus. In (37),  $\varepsilon^e = \varepsilon_{ij}^e = (u_{i,j} + u_{j,i})/2$  is the small strain tensor and  $u$  is the soil displacement. A detailed poro-elastic model for wave-induced soil responses around breakwater heads can be found in (Li and Jeng, 2008).

It is noted that the constitutive model, the Pastor–Zienkiewicz model, doesn’t consider the degree of rotation of principal stress axis induced in the seabed soil. Such an effects will becomes significant depending on wave form, as reported in Sassa and Sekiguchi (2001).

### 2.3 Boundary conditions

Appropriate boundary conditions are required to solve the abovementioned governing equations for soil-fluid interactions. First, because the surface of the seabed interacts directly with water, the wave-induced pore pressure equals the water pressure on the seabed surface. Meanwhile, the vertical effective normal stress and shear stress are assumed to be zero:

$$p = p_b = p_d + p_s, \quad \sigma'_z = \tau_{rz} = \tau_{\theta z} = 0 \quad \text{at } z=0 \quad (39)$$

where  $p_s$  is the static water pressure and  $p_d$  is the dynamic wave pressure given by (12).

Next, the bottom of the seabed is assumed to be impermeable and rigid. Therefore, there is no displacement or vertical flow on the bottom:

$$\frac{\partial p}{\partial z} = u_r = u_\theta = u_z = 0, \quad \text{at } z=-h \quad (40)$$

Third, a rigid boundary condition is assumed along the boundary of the domain. In previous research, the computational domain has usually been set with the radius of the computational domain  $R$  equal to one wavelength (Li and Jeng, 2008). Theoretically,  $R$  should be set as large as possible to simulate wide ocean environments. On the other hand, wave-induced liquefaction behaves most obviously around breakwater heads, where  $R$  is small. However, no work has been performed to discover how  $R$  affects numerical results, which is discussed in this paper.

The DYNE3WAC program has been extended from the two-dimensional model, DIANASWANDYNE II (Chan, 1995), to three dimensions (Ou, 2009). This model has recently been applied to investigate the regular wave-induced soil responses around breakwater heads (Jeng and Ou, 2010). We applied the model to random wave-induced seabed responses.

### 2.4 Finite element formulations

In this study, the finite element model of a seabed model (DYNE3WAC) was further extended to random wave-induced seabed responses. The spatial discretisation involved variables and was achieved by using suitable shape functions, given as:

$$u \gg u^h = \sum_{k=1}^n N_k^u \bar{u}_k = N^u \bar{u} \quad (41)$$

$$p \gg p^h = \sum_{k=1}^n N_k^p \bar{p}_k = N^p \bar{p} \quad (42)$$

where  $u^h$  and  $p^h$  are the numerical approximations to  $u$  and  $p$ , respectively.  $u$  is the nodal displacement variable vector and  $p$  is the nodal pressure variable. The matrix form of the consolidation form of the  $u$ - $p$  governing equations can be expressed as:

$$\int_W B^T S' dW - Qp = f^u \quad (43)$$

$$Q^T \dot{u} + Sp + Hp = f^p \quad (44)$$

$$B = \begin{matrix} \hat{\varepsilon} \\ \hat{\varepsilon} \end{matrix} \begin{matrix} \int \int \int \int \\ \int \int \int \int \end{matrix} \begin{matrix} \int \int \int \int \\ \int \int \int \int \end{matrix} \begin{matrix} 0 \\ 0 \\ 0 \\ \int \int \int \int \\ 0 \\ \int \int \int \int \\ 0 \\ \int \int \int \int \\ \int \int \int \int \\ \int \int \int \int \end{matrix} N^u \quad (45)$$

$$S = \int_W (N_p)^T \left( \frac{n}{K_f} + \frac{a_n}{K_s} \right) N^p dW \quad (46)$$

$$H = \int_W (\nabla N^p)^T \frac{k}{r_f g} \nabla N^p dW \quad (47)$$

$$Q = \int_W B^T a m N^p dW \quad (48)$$

$$f^u = \int_W (N^u)^T r b dW + \int_{G_i} (N^u)^T \bar{t} dG \quad (49)$$

$$f^p = - \int_W (N^p)^T (k r_j b) dW + \int_{G_i} (N^p)^T \bar{q} dG \quad (50)$$

in which  $\bar{q}$  is the prescribed influx and  $\bar{t}$  is the prescribed traction on the boundary.

To complete the numerical solution, it was necessary to integrate the ordinary differential equations (43) and (44) in the time domain. The current model employed the single-step generalised Newmark ( $GN_{pi}$ ) method (Wood, 1990). Using  $GN_{11}$  for both the nodal displacements and the nodal pore pressures, we write:

$$\dot{u}_{n+1} = \dot{u}_n + D \dot{u}_n \quad (51)$$

$$u_{n+1} = u_n + \dot{u}_n Dt + d_1 D \dot{u}_n Dt \quad (52)$$

$$\dot{p}_{n+1} = \dot{p}_n + D \dot{p}_n \quad (53)$$

$$p_{n+1} = p_n + \dot{p}_n Dt + \bar{d}_1 D \dot{p}_n Dt \quad (54)$$

The unconditional stability of the recurrence scheme requires that

$$d_1 \geq 1/2 \quad \text{and} \quad \bar{d}_1 \geq 1/2.$$

### 2.5 Determination of random wave parameters

To ensure the accuracy of the simulated random waves, the number of Bessel Function terms  $M_b$  and wave components  $M_r$ , as shown in (10) and (12), were two key parameters. In principle, they should be as large as possible. However, calculation efficiency and effectiveness demand a balance between time costs and simulation accuracy, and both parameters were therefore set to suitable values.

Among these two parameters,  $M_b$  relates directly to the stability of each wavelet, so it should be analysed first. As seen in (10), the parameters  $r$ ,  $\theta$  and wave period  $T$  can influence the determination of the number of Bessel Function terms. Figure 3, Figure 4 and Figure 5 show how these parameters affect the convergence of the water elevation  $\eta$ . In general,  $\eta$  tends to converge easily for regular waves with  $M_b \approx 5$ . As shown in Figure 3, a larger value of  $M_b$  is required for  $\eta$  to converge as the radius increases. To ensure that the simulation results converge over the entire domain under study,  $M_b$  should be set at approximately 40 for random waves.

Similarly, Figure 4 reveals that the minimum value of  $M_b$  should also be approximately 40, including for random waves. Furthermore, the figures demonstrate that the minimum  $M_b$  must be 45 to satisfy the different positions compared to  $\theta$  (Figure 5). Comparing Figs. 3-5 shows that  $M_b = 5$  can provide sufficient accuracy with regular waves, while  $M_b = 45$  is required for good accuracy with random waves. These results were attributed to the irregularity of random waves, meaning that more Bessel Function terms were required for both JONSWAP and B-M random waves.

The second parameter that significantly affected the simulation results was the wave component  $M_r$ . In Figure 6 and Figure 7, the water elevation  $\eta$  is plotted versus time and proves that the required minimum number of wave components is approximately 25. Hence,  $M_r$  was set to 25 in the numerical program.

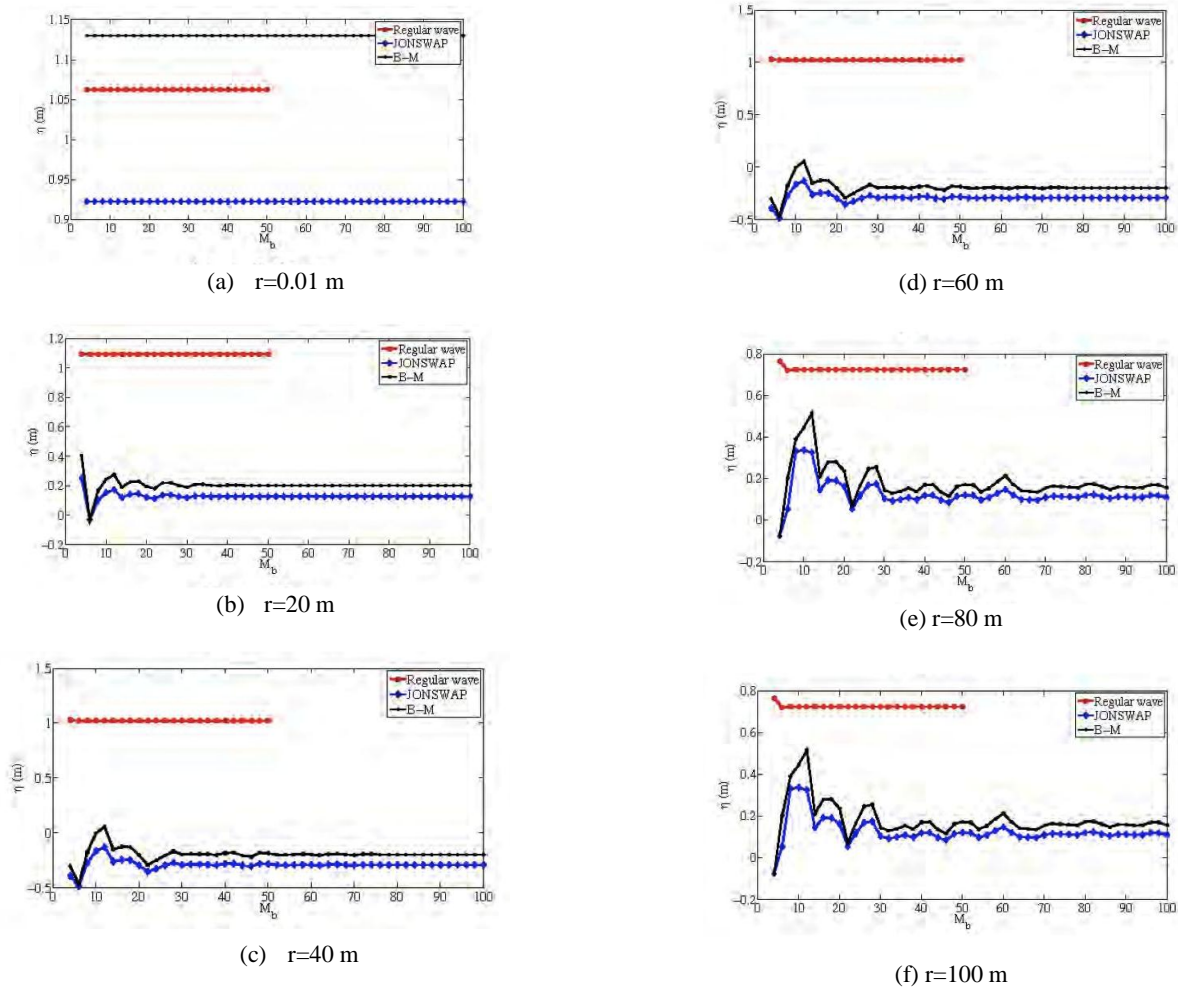
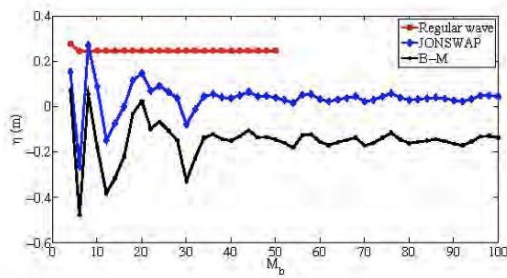
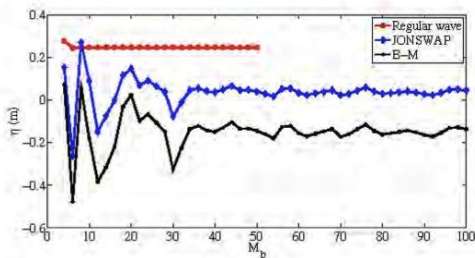


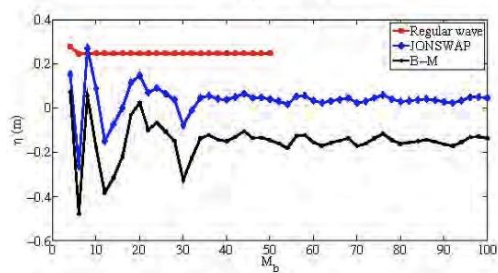
Figure 3 Water elevation variations with  $M_b$  at different locations ( $\theta=135^\circ$ ,  $\alpha=135^\circ$  and  $T_{1/3}=10$  seconds).



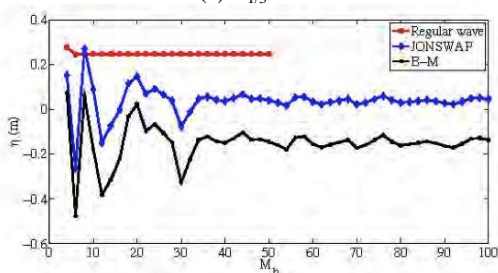
(a)  $T_{1/3} = 5$  s



(b)  $T_{1/3} = 7.5$  s

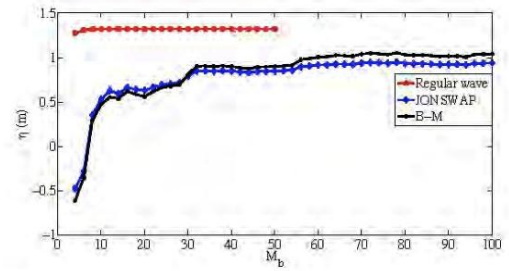


(c)  $T_{1/3} = 10$  s

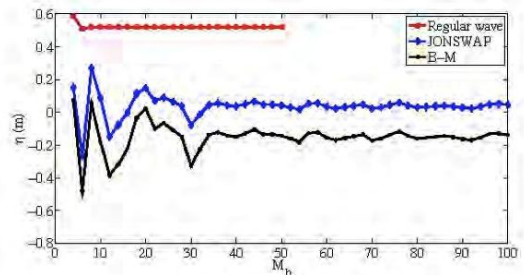


(d)  $T_{1/3} = 12.5$  s

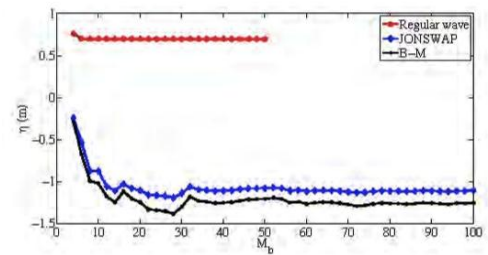
Figure 4 Water elevation variations with  $M_b$  for a representative wave period ( $\theta=135^\circ$ ,  $\alpha=135^\circ$  and  $r=0.01$  m)



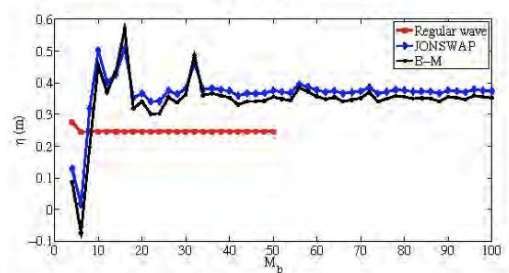
(a)  $\theta=45^\circ$



(b)  $\theta=135^\circ$



(c)  $\theta=270^\circ$



(d)  $\theta=315^\circ$

Figure 5 Water elevation variations with  $M_b$  at different locations ( $r=100$  m,  $\alpha=135^\circ$  and  $T_{1/3}=10$  seconds)

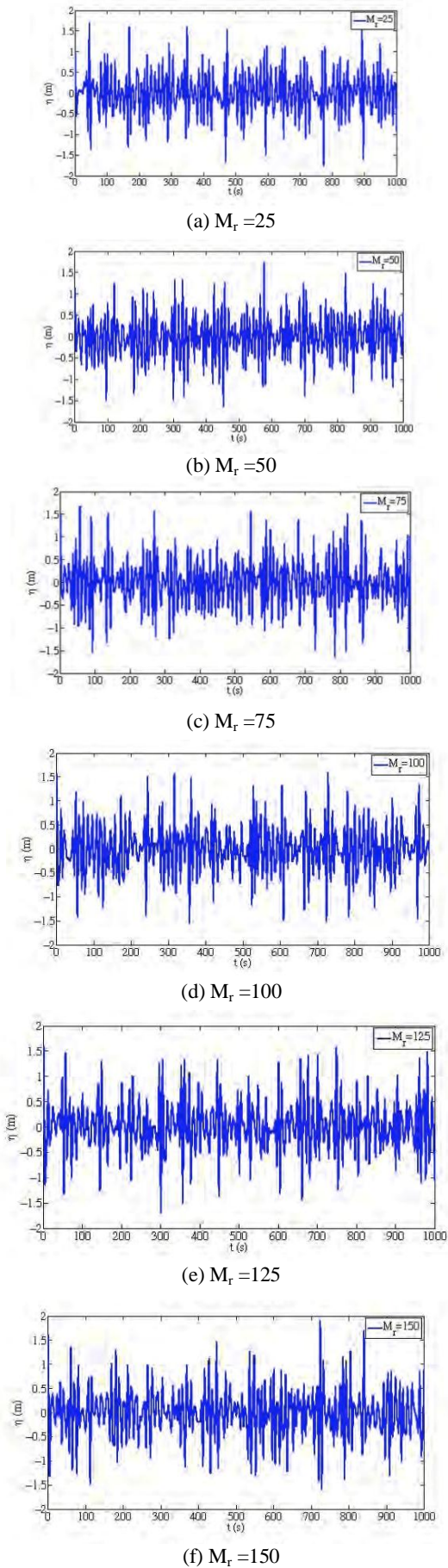


Figure 6 Water elevation variations for various wave components (JONSWAP spectrum,  $r=0.001$  m,  $\theta=135^\circ$ ,  $\alpha=135^\circ$  and  $T_{1/3}=10$  seconds).

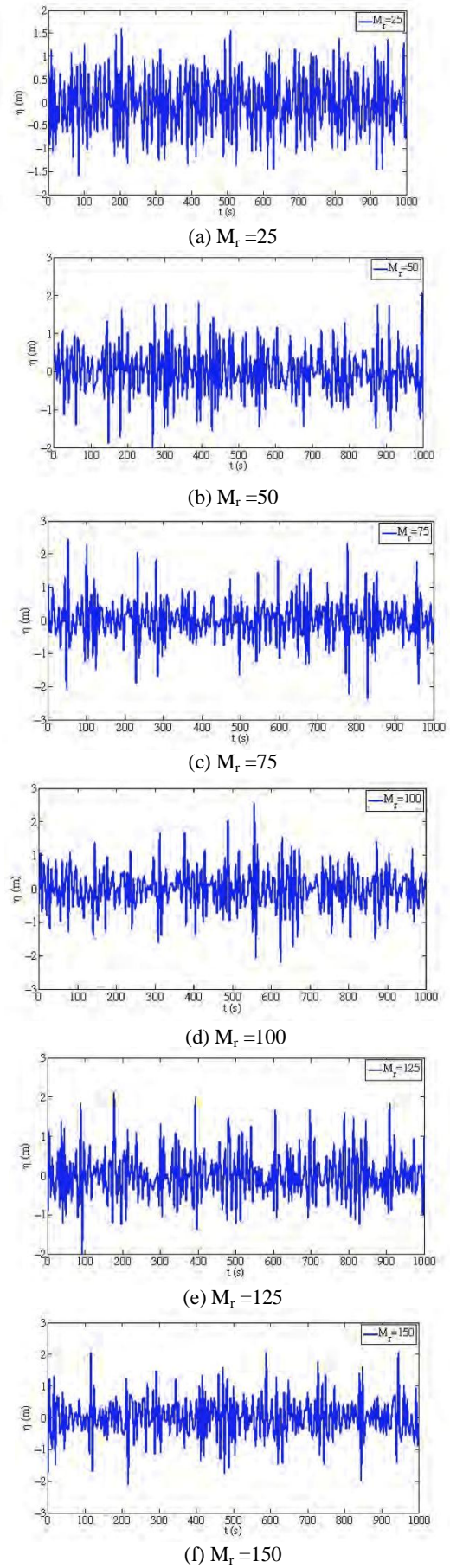


Figure 7 Water elevation variations for various wave components (B-M spectrum,  $r=0.001$  m,  $\theta=135^\circ$ ,  $\alpha=135^\circ$  and  $T_{1/3}=10$  seconds)

**2.6 Convergence of meshes**

When the mesh is too coarse, the size of each element inside may be too large and result in divergence during calculation. Hence, convergence tests were performed to determine the minimum number of elements required for convergence. Figure 8 illustrates the mesh we used in the numerical examples, plotted in the Cartesian coordinate system. The origin lies on the bottom of the mesh with the z-axis in the upward direction. Therefore, when the seabed thickness was  $h$ , points on the top had  $z=h$ . In addition, the mesh was developed to different degrees of fineness in the  $r$ -direction (viewed in the corresponding cylindrical coordinate system) and the  $z$ -direction, which was in reaction to the demand that zones around breakwater heads be investigated in more detail.

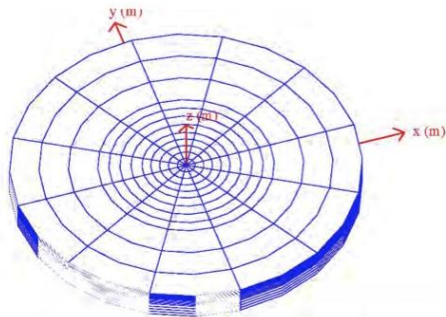


Figure 8 Newly developed mesh applied in the DYNE3WAC program

Four different numbers of elements (i.e., 640, 1200, 1440 and 2304) were selected for comparison with the random wave-induced pore pressure at the fixed point,  $r=0.375L_c$ ,  $\theta=0^\circ$  and  $z=10$  m. Note that  $L_c$  is the wavelength determined by the representative wave period and water depth. The results are presented in Figure 9(a). Because 27 nodal cube elements, which brought the model up to the second-order approximation, were used in this study's calculations, the number of elements did not need to be large. Finer meshes were used in the region near the breakwater heads and coarser meshes were used in the region far from the breakwaters by implementing an exponential function.

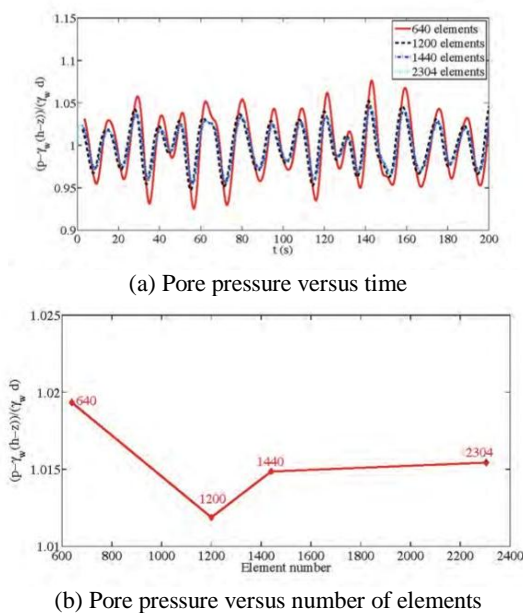


Figure 9 Normalised wave-induced pore pressure variations with (a) time and (b) number of elements, at the point  $r/L=0.375$ ,  $\theta=0^\circ$  and  $z=10$  m.

The figure shows that when the element number increases from 640 to 1200, the time-varying pore pressure changes significantly. A further increase in the number, however, to 1440, should not be neglected. By comparing the results obtained with 1440 and 2304 elements, we found that the two corresponding lines overlapped closely. Figure 9(b) demonstrates the element convergence by comparing the pore pressure at the same location and time point. Therefore, it was concluded that the mesh had already reached a state of convergence when the number of elements was only 1440. However, 2304 elements were selected for the following analysis to ensure there would be enough nodes in the mesh to describe a wave-induced soil response.

**2.7 Boundary scale**

In principle, the domain for breakwaters in ocean environments is supposed to be infinite along the  $r$ -direction. However, it is impossible to perform simulations in the finite element program without fixing a boundary in the  $r$ -direction. It is also unnecessary to set the boundary to infinity due to the structure's minimal influence on the soil response when  $R$  is sufficiently large. We used three different boundary sizes,  $R/L_c=1, 0.75$  and  $0.5$ , and compared them to determine an optimal scale for the boundary in the  $r$ -direction. Figure 10 demonstrates that the three groups of pore pressure variations are in accordance with one another. However, a tiny difference between  $R/L_c=0.75$  and  $0.5$  can still be observed. The results for  $R/L_c=1$  and  $0.75$  overlap perfectly, which means  $R$  does not play a role in influencing the wave-induced pore pressure around breakwater heads when it is greater than  $0.75L_c$ . Nonetheless,  $R/L_c=1.0$  was still adopted for analysis because wave-induced pore pressure could behave differently when the point is below different phase of waves with  $L_c$ .

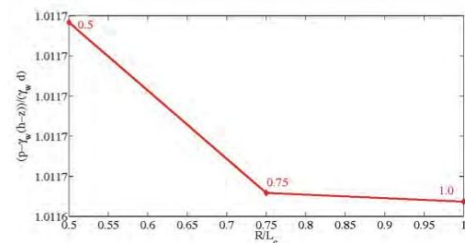


Figure 10 Normalised wave-induced pore pressure at a fixed location and time point ( $z=10$  m,  $r/L=0.05$ ,  $\theta=135^\circ$  and  $t=199$  s)

**2.8 Comparison with previous studies**

Because there are no experimental data on wave-seabed interactions around breakwater heads available in the literature, the present model could be validated only by considering special cases reported in previous studies. First, the present model was compared with the 2D experimental data (Vun, 2005), as shown in Figure 11. Considering a homogeneous seabed subject to a progressive wave loading, the pore pressure predicted by the elasto-plastic model is compared with the previous experimental data obtained by Vun (2005) in the figure. Figure 11 shows the results at 0.085 m below the seabed surface in the test. It was found that, with the proper material parameters used by Vun (2005), the present numerical model provided a good overall prediction of both residual and oscillatory pore pressure fluctuations in the seabed.

The current model was next compared with the analytical solution for the 3D short-crested wave-induced soil response (Figure 12). Note that the analytical solution (Hsu and Jeng, 1994) applies only to the case in front of a breakwater, not around breakwater heads. The linear elastic constitutive model was used instead of the poro-elastoplastic model to compare the model with the analytical solution. The design wave condition in the North Sea was used as an example, with a water depth of 70 m and a wave

height of 5m. The shear modulus and Poisson’s ratio of the seabed were taken as 10MPa and 1/3, respectively. The soil porosity was 0.3 and the permeability was taken as 0.01 m/s. Nine hundred 27-noded Lagrangian brick elements were used in the analysis. There was excellent agreement between the numerical model (solid lines) and the analytical solution (symbols), as shown in Figure 12.

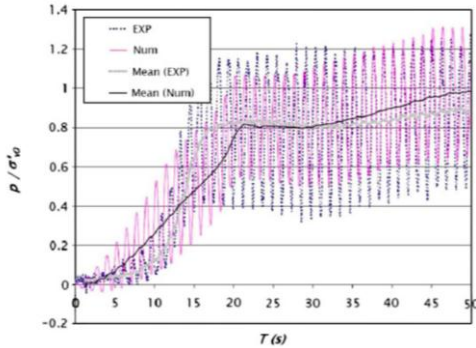


Figure 11 Comparison between the current numerical predictions and experimental data (Vun, 2005) on the pore pressure at 0.085 m below the seabed surface.

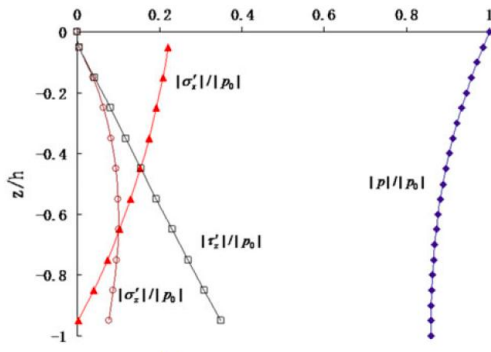


Figure 12 Comparison between the 3D analytical solution (Hsu and Jeng, 1994) and the current model (reduced to a linear poro-elastic mode) for the case in front of a breakwater.

A simple study on the regular wave-induced soil response around breakwater heads by the first author and his co-worker (Jeng and Ou, 2010; Ou, 2009) was then examined so that a comparison with the previous model could be made to verify the current mesh. Three different water depths (*d*) were chosen: 2.45 m, 8.69 m and 26.55m. When the wave period (*T*) was set 10 s, the *d/L* values were 0.05, 0.1 and 0.2, respectively. Detailed wave conditions and soil properties are tabulated in Table 1 and Table 2.

Figure 13 presents a comparison of the time history of the wave-induced pore pressure and residual pore pressure at three different depths in the seabed. When the point is located on the bottom of the finite seabed (Figure 13a and Figure 13b), both Ou’s model (Ou, 2009) and the current results obtained with the new mesh show an approximately constant pore pressure amplitude over time (a) and are of a similar value. Meanwhile, the residual pore pressure (b) increases gradually with time. However, the new simulation shows comparatively faster accumulation of excess pore pressure. Upon further inspection of the pore pressure between the two, the difference is found to be controlled below 20%. A similar behaviour takes place at the point *z*=10m (Figure 13c and Figure 13d) and the difference is less than 10%. The wave-induced pore pressure at the location on the seabed surface is directly affected by the dynamic water pressure. Therefore, the oscillatory excess pore pressures are the same (Figure 13e). It appears that the residual pressures behave differently. If the exact values are checked, the difference is tiny and is in fact due to the difference values of gravitational acceleration

(9.81 kN/s<sup>2</sup> and 9.806 kN/s<sup>2</sup>). As seen in Figure 14 and Figure 15, the new simulations with *d*=8.69m and 2.45m, respectively, agree reasonably well with the previous model (Ou, 2009).

It is worth mentioning that the initial loading used in the previous work (Jeng and Ou, 2010; Ou, 2009) is exerted gradually, so it takes some time to reach a stable state. This phenomenon is more obvious in residual pore pressure on the seabed surface. In summary, the above comparison demonstrated that the newly developed mesh could be verified and further applied to the analysis of wave-induced pore pressure in the next chapter.

Table 1 Wave conditions used in the comparisons

Test No.	<i>D</i> (m)	<i>T</i> (m)	<i>H</i> (m)	<i>d/Lc</i>
P1-1	2.45	10	0.98	0.05
P1-2	8.69	10	2.61	0.1
P1-3	26.55	10	2.65	0.2

Table 2 Selected parameters used in the PZ - III model during the comparison study

Parameter	Unit	Value	Parameter	Unit	Value
<i>M<sub>r</sub></i>	-	1.15	<i>H<sub>u0</sub></i>	kPa	40000
<i>M<sub>f</sub></i>	-	1035	<i>γ<sub>u</sub></i>	-	2.0
<i>α<sub>f</sub></i>	-	0.45	<i>γ<sub>DM</sub></i>	-	0
<i>α<sub>g</sub></i>	-	0.45	<i>ν</i>	-	0.31
<i>H<sub>ev0c</sub></i>	-	770	<i>K</i>	m/s	0.001
<i>H<sub>es0c</sub></i>	-	1155	<i>P<sub>a</sub>'</i>	kPa	4
<i>β<sub>0</sub></i>	-	4.2	<i>G<sub>s</sub></i>	-	2.65
<i>β<sub>1</sub></i>	-	0.2	<i>e</i>	-	0.8
<i>H<sub>0</sub></i>	kPa	600	<i>γ</i>	N/m <sup>2</sup>	18802.51

### 3. NUMERICAL RESULTS AND DISCUSSION

#### 3.1 Comparison of random and regular waves

Unlike regular waves, which have specific *d*, *H* and *T* values, random waves behave irregularly. Therefore, random wave-induced pore pressure can be analysed only qualitatively. To compare different points with different soil depths, the figures are presented in a normalised manner to eliminate the effects of soil depth.

Figure 16 illustrates both the regular and corresponding random wave-induced pore pressures over time in a normalised manner. Although a similar trend can be observed in the random wave-induced pore pressure, the randomness dominates and makes the accumulation of pore pressure implicit compared to that of regular waves. Different locations (with a fixed *r* but varying *θ*) were selected, 45°, 135°, 225° and 315°, which represent the four zones introduced in Figure 1. Figure 16 reveals the differences in wave-induced pore pressures at different locations based on *θ*. When *r/Lc*=0.05, the pore pressures introduced by both the regular and random waves are similar. However, as *r/L* increases, the differences become obvious (graphs not shown). The smallest amplitude of wave-induced pore pressure occurs when *θ*=315° because only scattered waves *T* can affect the soil response. Similar behaviour occurs at the location with *θ*=45° (graph not shown), where the incident and reflected waves combine with each other. Once again, it is noteworthy that the irregularity of the random waves tends to make the pore pressure development ambiguous.

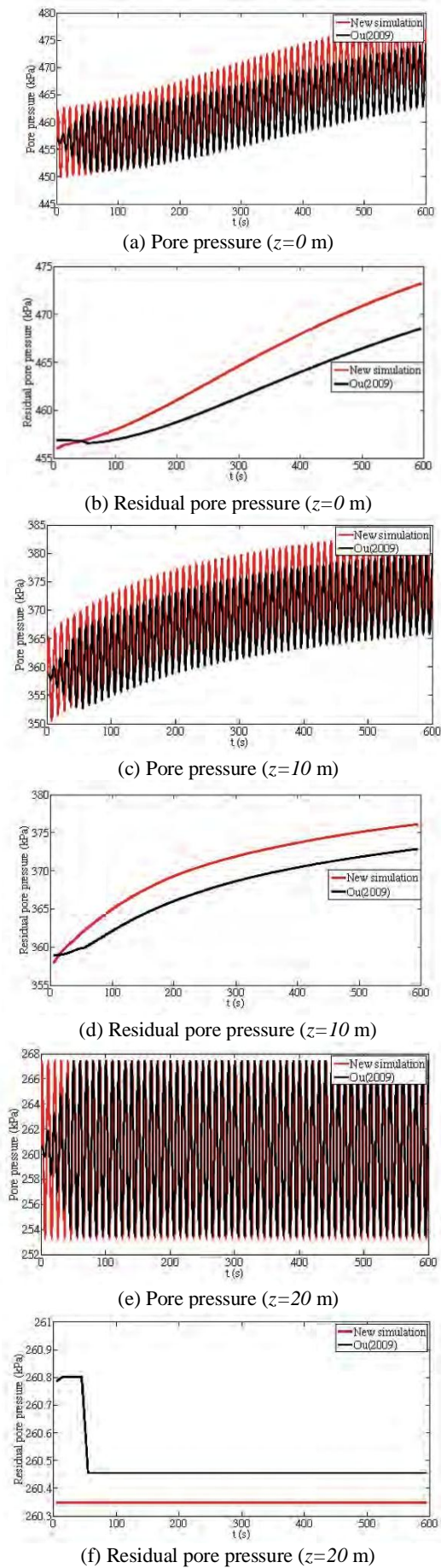


Figure 13 Wave-induced pore pressure or residual pore pressure over time at various locations ( $d=26.55$  m)

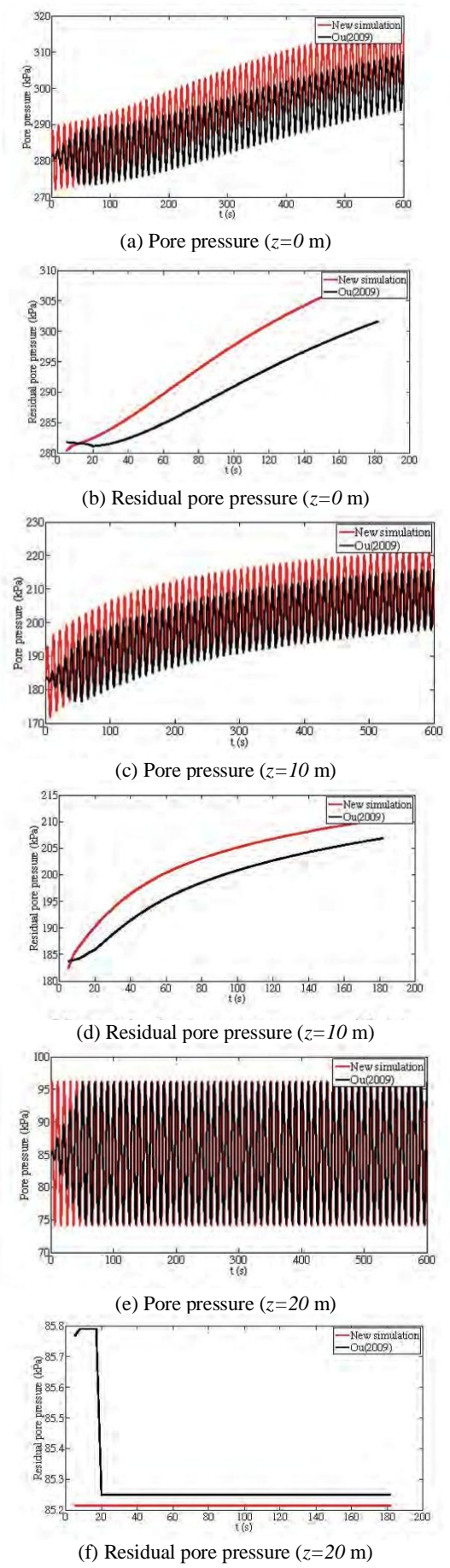


Figure 14 Wave-induced pore pressure or residual pore pressure over time at various locations ( $d=8.69$  m)

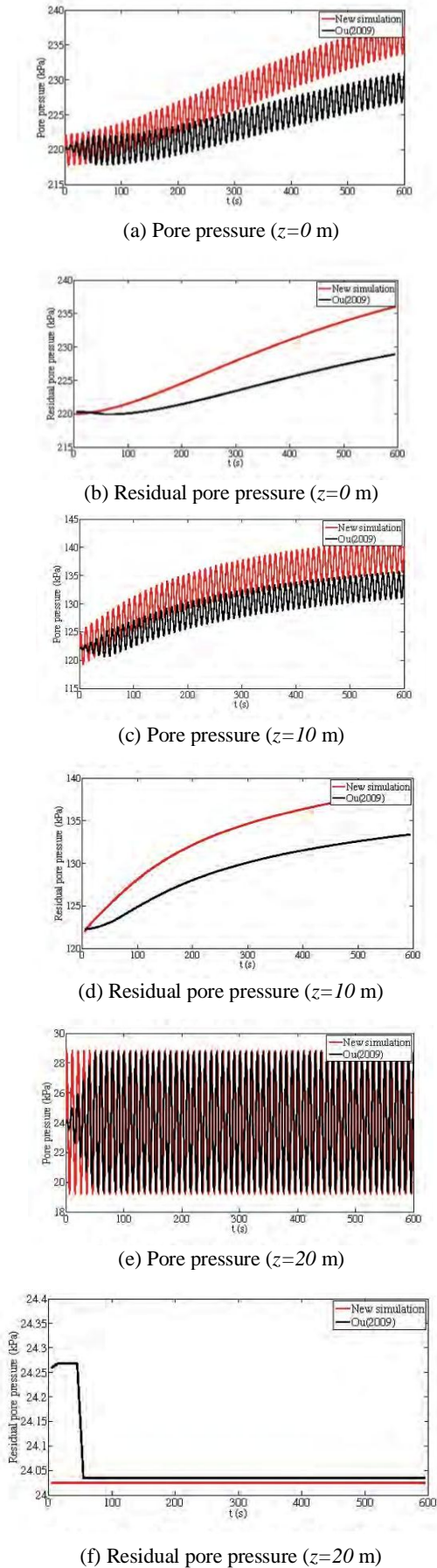


Figure 15 Wave-induced pore pressure or residual pore pressure over time at various locations ( $d=2.45$  m)

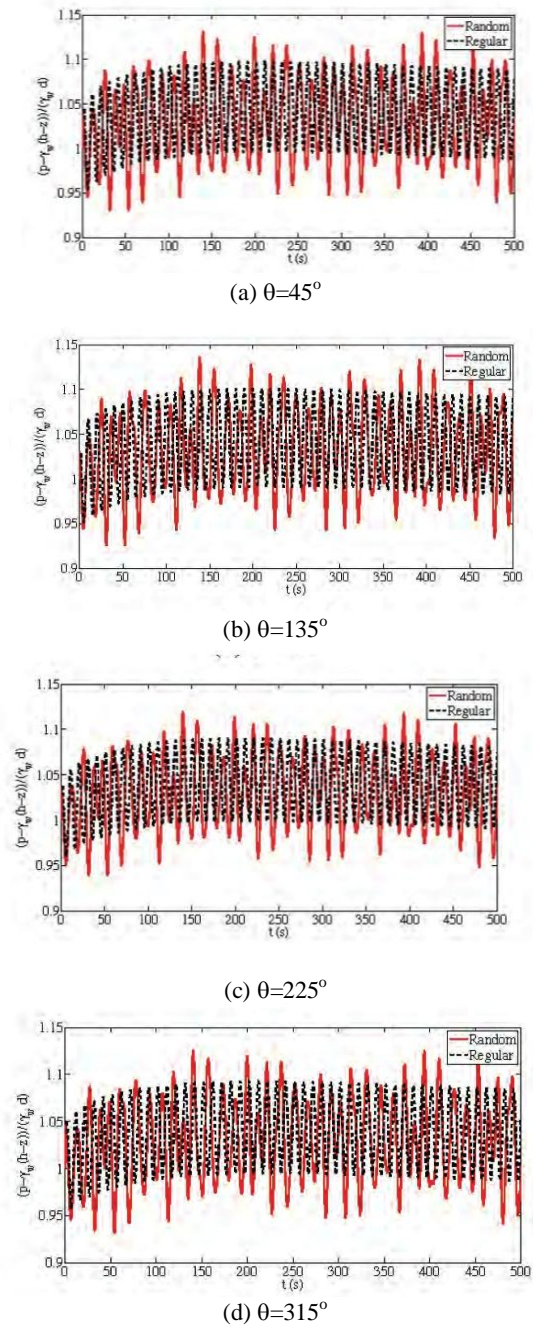


Figure 16 Normalised wave-induced pore pressure over time at various locations ( $\alpha=135^\circ$ ,  $d=15$  m,  $T=10$  s,  $H/Lc=0.03$ ,  $k=0.01$  m/s)

### 3.2 Comparison of poro-elastic and poro-elastoplastic models

This section compares two groups of results, one from the elastoplastic model and another from the elastic model. The wave and seabed conditions were  $\alpha=135^\circ$ ,  $d=15$  m,  $T=10$  s,  $H/Lc=0.03$  and  $k=0.01$  m/sec. As shown in Figure 17 and Figure 18, the wave-induced pore pressures from the elastoplastic model behaved at higher amplitudes and the pore pressures accumulated more obviously when the plasticity of soil was taken into account. When pore pressures at different soil depths were compared, we found that the difference in pore pressures between the models increased as the soil depth increased. Figure 19 presents the pore pressure variations with different  $r$  values and demonstrates that  $r$  had a tiny influence on the differences in the results from both models. A similar trend was found for  $\theta$  (Figs. 18 and 19).

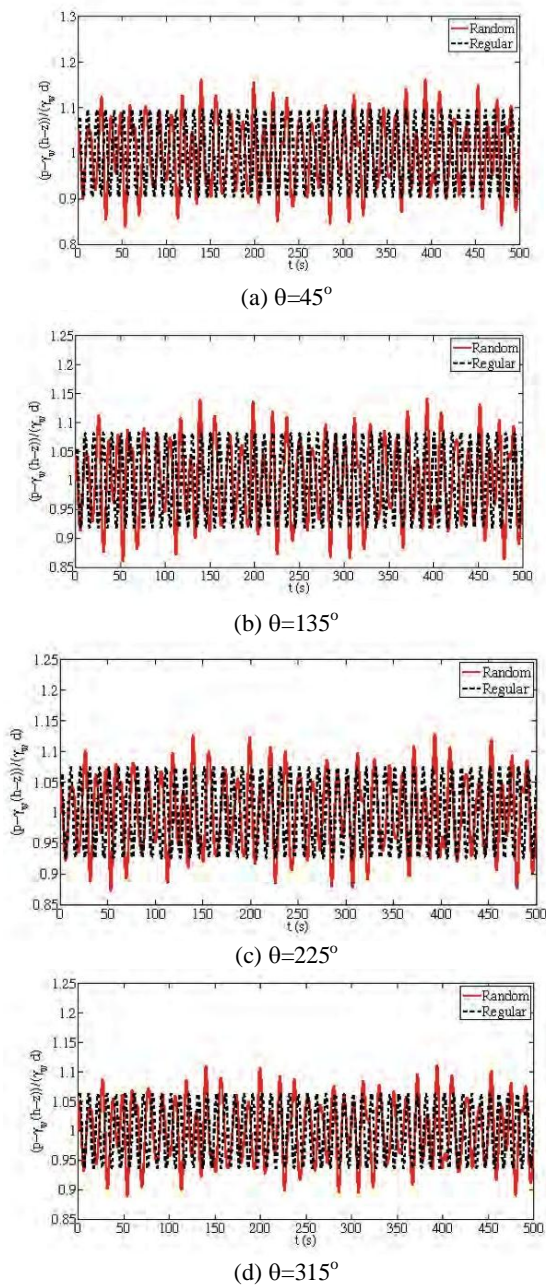


Figure 17 Normalised wave-induced pore pressure over time at various points based on  $\theta$  ( $z=0$  m,  $r/Lc=0.05$ )

In general, the soil strain could be divided into two parts: elastic strain (reversible) and plastic strain (irreversible). Based on soil-fluid interaction theory, the volumetric strain change in soil influences the storage capacity in pores, thereby affecting pore pressure. By introducing the plastic part of strain in the elasto-plastic model, the storage capacity of soil in pore was significantly improved and led to an apparent difference in pore pressure between the elasto-plastic and elastic models.

### 3.3 Effects of wave characteristics

Three essential parameters are used to define waves: time period ( $T$ ), wave height ( $H$ ) and wave length ( $L$ ).  $L$  is actually related to  $T$  and water depth ( $d$ ) in water areas. Therefore,  $d$ ,  $H$  and  $T$  were studied here. Because the implemented wave system was 3D short-crested, the wave obliquity relative to the breakwater could have significant effects on the wave-induced pore pressure and was therefore worth studying as well.

In general, two special cases can be considered for water areas.

When  $d/Lc=0.5$ , it is taken as deep water.

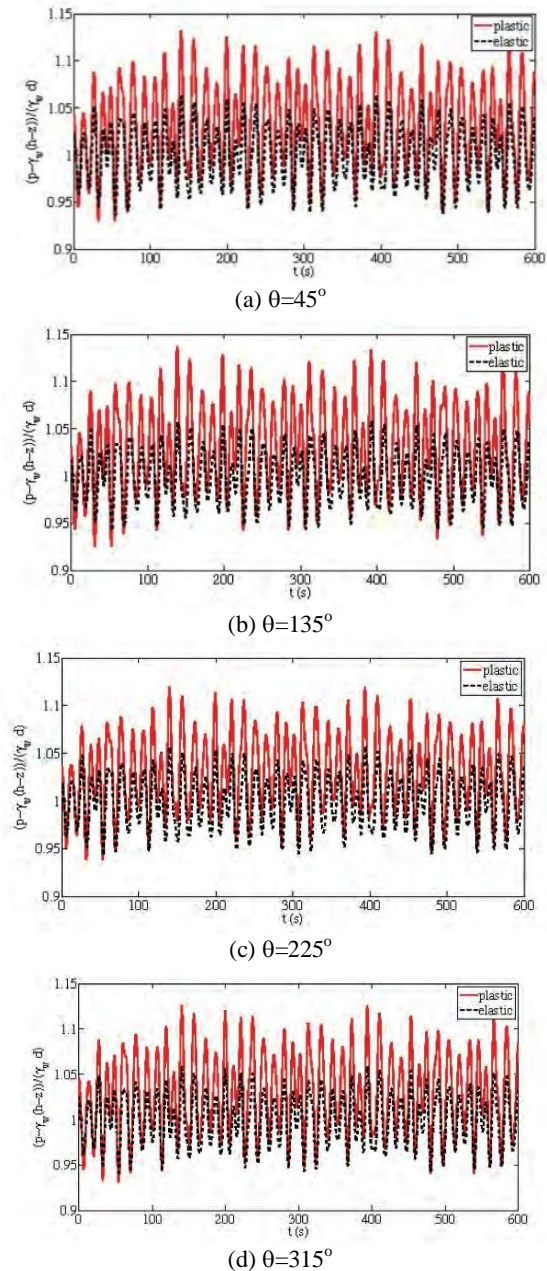


Figure 18 Normalised wave-induced pore pressure over time at various points based on  $\theta$  ( $z=10$  m,  $r/Lc=0.05$ )

As mentioned previously,  $Lc$  is the wavelength determined by the representative wave period and water depth. On the other hand, shallow water is introduced when  $d/Lc=0.05$ . Most breakwaters are located in areas of intermediate water with  $0.05 < d/Lc < 0.5$ . Three different water depths were introduced to the analysis,  $d=5$  m, 15 m and 25 m, which corresponded to  $d/Lc=0.0739$ , 0.147 and 0.192, respectively, with a fixed characteristic regular wave period of  $T_c=10$  s.

As illustrated in Figure 20, the water depth had a clear influence on the magnitude of the wave-induced pore pressure. In other words, the magnitudes of pore pressure at various points increased dramatically as  $d/Lc$  decreased. The difference in the pore pressure magnitude was up to one order higher for  $d/Lc=0.0739$  compared to  $d/Lc=0.192$ . This phenomenon was attributed to the more obvious dynamic wave pressure on the seabed surface in shallow water, which led to correspondingly significant variations in pore pressure. Meanwhile, a clear trend in pore pressure accumulation was observed in shallow water ( $d/Lc$ ). Therefore, it was concluded that the soil below the foundation was apt to experience liquefaction in

shallow water areas where  $d/L_c$  was small.

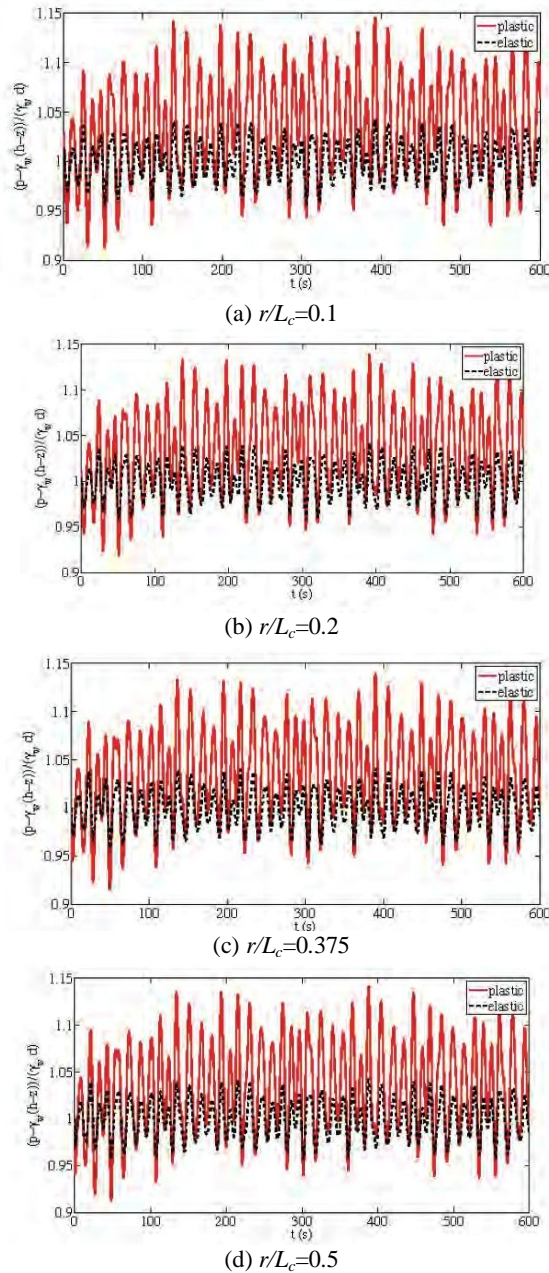


Figure 19 Normalised wave-induced pore pressure over time at various points based on  $\theta$  ( $z=10$  m,  $\theta=135^\circ$ )

Wave height is another important parameter during the design of marine structures. It has been demonstrated (Li and Jeng, 2008) that wave steepness ( $H/L$ ) significantly affects pore pressure buildup. Specifically, the equilibrium pore pressure increases as the wave steepness increases. In this study, three different wave steepness of  $H/L_c=0.03, 0.05$  and  $0.07$  were selected. As shown in Figure 21, the wave steepness had a significant influence on the amplitude of the wave-induced excess pore pressure. As the wave steepness increased, the amplitude of the wave-induced pore pressure increased significantly. Further inspection of Figure 21 shows a slight difference in pore pressure accumulation with different characteristic wave steepnesses. The rate of accumulation of excess pore pressure increased as the characteristic wave steepness increased, and the difference was insignificant because the soil had a high permeability ( $k$ ). With low permeability, the difference in the accumulation rate was amplified.

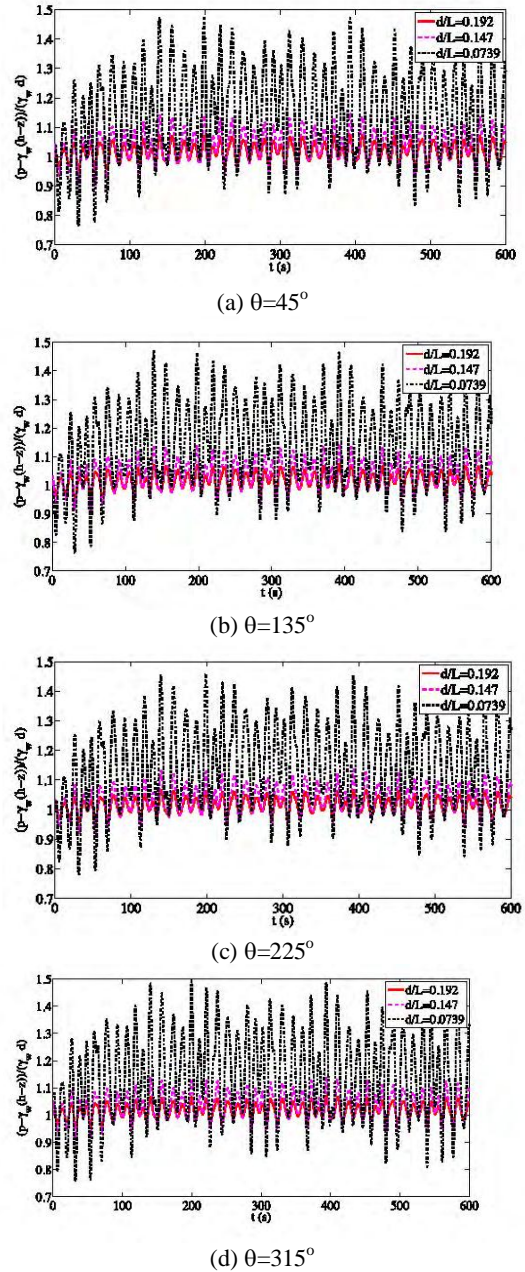
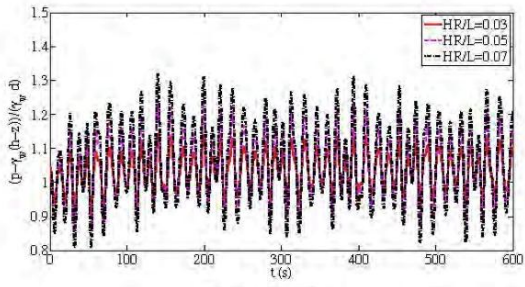


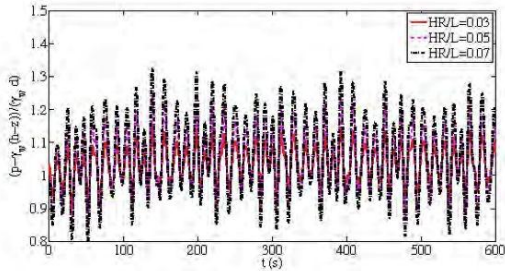
Figure 20 Normalised wave-induced pore pressure over time for various relative water depths ( $d/L$ ) at different locations, with points based on  $\theta$  ( $z=10$  m,  $r/L_c=0.05$ ).

The wave period is another vital wave parameter and cooperates with water depth to determine the wavelength. Li and Jeng (2008) have noted that both the magnitude and equilibrium value of pore pressure increase as the wave period decreases, which is attributed to the high frequent accumulation of pore pressure, thereby leading to relatively slow dissipation.

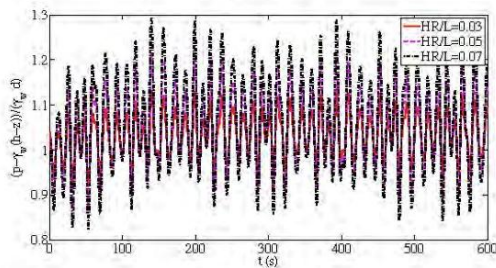
Three different characteristic wave periods ( $T_c$ ) were used in this study: 12.5 s, 10 s and 7.5 s. The comparison results are presented in Figure 22. Generally speaking, the influence of the wave period on the wave-induced pore pressure appeared to be less obvious than that of other parameters. However, a general trend still existed, with the amplitude of pore pressure increasing as the wave period increased. It was also observed that the peak pore pressures for each wave period stayed at the same level, whilst the lower



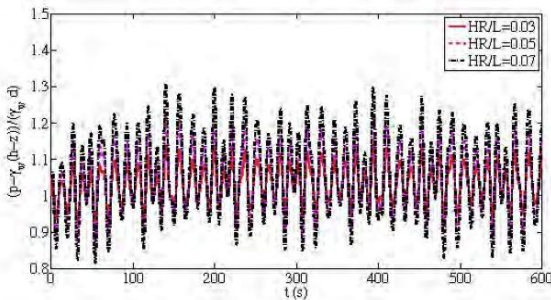
(a)  $\theta=45^\circ$



(b)  $\theta=135^\circ$



(c)  $\theta=225^\circ$



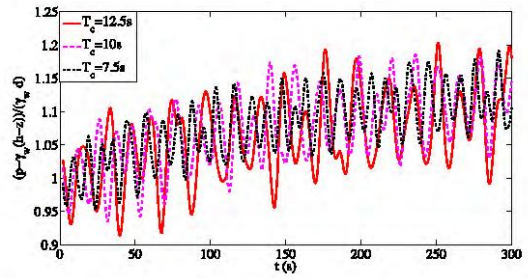
(d)  $\theta=315^\circ$

Figure 21 Normalised wave-induced pore pressure over time for various wave steepnesses ( $H/L$ ) at different locations, with points based on  $\theta$  ( $z=10$  m,  $r/Lc=0.05$ )

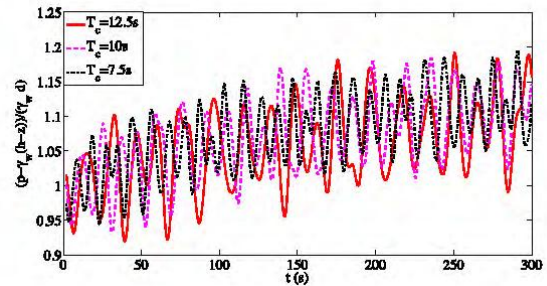
troughs, pore pressures for longer wave periods possessed relatively meaning that the residual pore pressures increased as the wave period decreased. The reasons for this behaviour have been revealed by Li and Jeng (2008) and were briefly introduced above.

Wave obliquity is taken into account only in 3D cases. The existing research (Li and Jeng, 2008; Jeng, 1996) has indicated that the incident wave angle ( $\alpha$ ) directly affects both the magnitude and the distribution of wave-induced liquefaction at the tip of a breakwater. Moreover, it has been specifically revealed that  $\alpha = 45^\circ$  leads to a comparatively obvious soil response around breakwater heads.

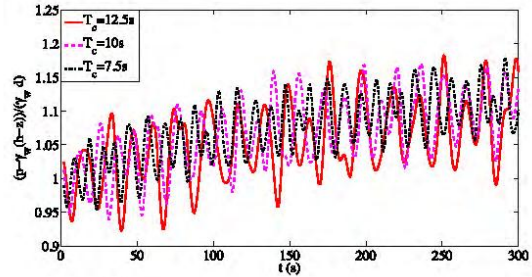
Because the soil domain was symmetrical along the breakwater, it was not necessary to study incident wave angles greater than  $180^\circ$ .



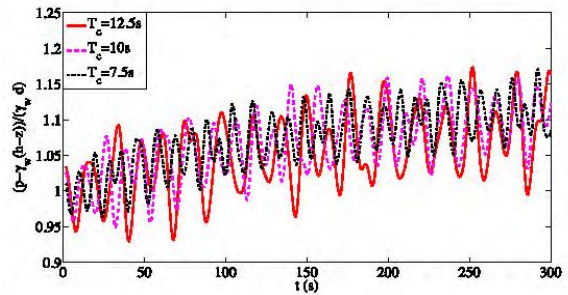
(a)  $\theta=45^\circ$



(b)  $\theta=135^\circ$



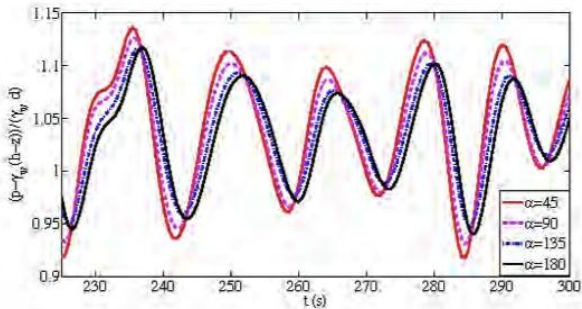
(c)  $\theta=225^\circ$



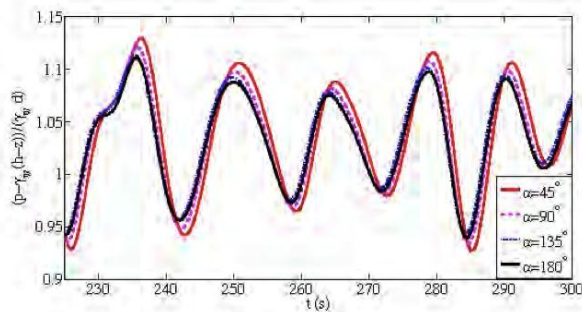
(d)  $\theta=315^\circ$

Figure 22 Normalised wave-induced pore pressure over time for various wave periods ( $T$ ) at different locations, with points based on  $\theta$  ( $z=10$  m,  $r/Lc=0.05$ )

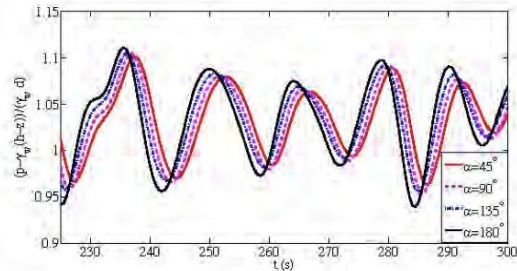
Four incident wave angles  $\alpha$  were chosen:  $45^\circ$ ,  $90^\circ$ ,  $135^\circ$  and  $180^\circ$ . As shown in Figure 23, the wave-induced pore pressure of a fixed location point had an amplitude that definitely varied with the wave angle. Specifically, the amplitude of the pore pressure in front of the structure decreased as  $\alpha$  increased (Figure 23a and Figure 23b). On the other hand, Figure 23c and Figure 23d show that the amplitude of pore pressure increased as  $\alpha$  increased, which has not been observed in a previous paper (Li and Jeng, 2008). Moreover, the difference in amplitudes at points with different  $\theta$  values became more apparent as  $\alpha$  decreased (graphs not shown). However, no significant influence was observed in the difference in pore pressure amplitudes along the  $r$ -direction (graphs not shown).



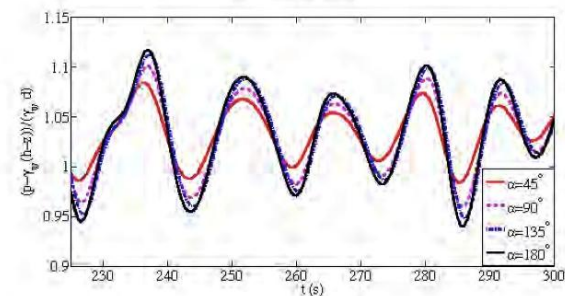
(a)  $\theta=45^\circ$



(b)  $\theta=135^\circ$



(c)  $\theta=225^\circ$



(d)  $\theta=315^\circ$

Figure 23 Normalised wave-induced pore pressure over time for various wave obliquities ( $\alpha$ ) at different locations, with points based on  $\theta$  ( $z=10$  m,  $r/Lc=0.05$ )

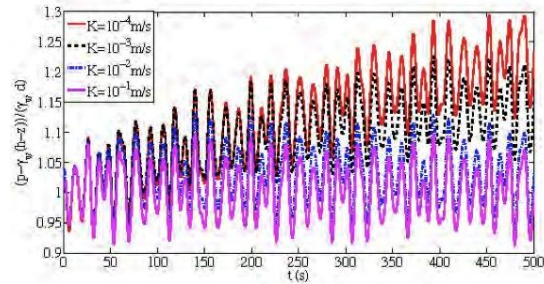
Therefore, the major conclusion for wave obliquity was that soil with a small wave angle ( $\alpha$ ) tended to produce extremely high amplitudes of pore pressure in certain areas, thereby leading to deep liquefaction depth. This conclusion should be taken into account during the design of breakwaters.

### 3.4 Effects of seabed characteristics

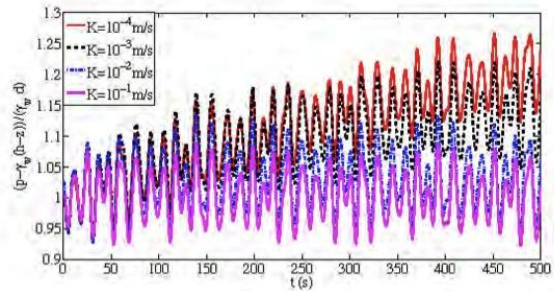
Soil permeability is an important factor affecting the drainage of pore fluid in soils. When soil permeability is low, the drainage of water in the seabed is impeded. Subsequently, excess pore pressure is generated without corresponding dissipation, leading to an obvious accumulation of excess pore pressure. On the other hand,

when soil permeability is high, the generation and dissipation of excess pore pressure tends to reach a balance, and thus little or no accumulation of pore pressure occurs.

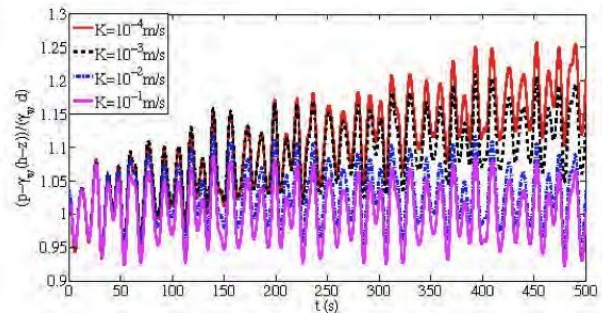
Four different soil permeabilities  $K$  were selected for this study:  $10^{-4}$  m/s,  $10^{-3}$  m/s,  $10^{-2}$  m/s and  $10^{-1}$  m/s. Figure 24 and Figure 25 reveal that the wave-induced pore pressure fluctuated at a roughly constant level for  $K=10^{-1}$  m/s and  $K=10^{-2}$  m/s. However, when  $K=10^{-3}$  m/s and  $K=10^{-4}$  m/s, a rapid increase over time was observed in the wave-induced pore pressure. The rate of excess pore pressure also accumulated faster as the soil permeability  $K$  decreased. It has been noted by Jeng and Hsu (1996) that the difference in pore pressure between permeabilities can be up to 40%. Because the adopted program was restricted to the study of soil responses in finite seabeds, the influence of seabed thickness on wave-induced pore pressure was a concern.



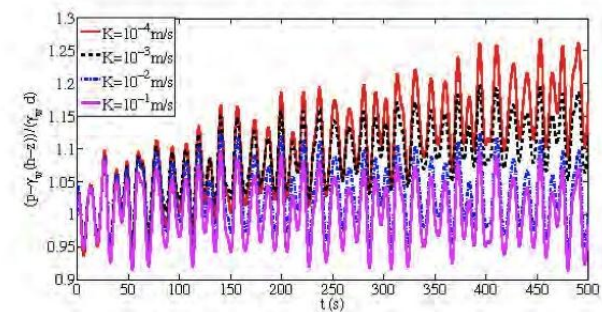
(a)  $\theta=45^\circ$



(b)  $\theta=135^\circ$

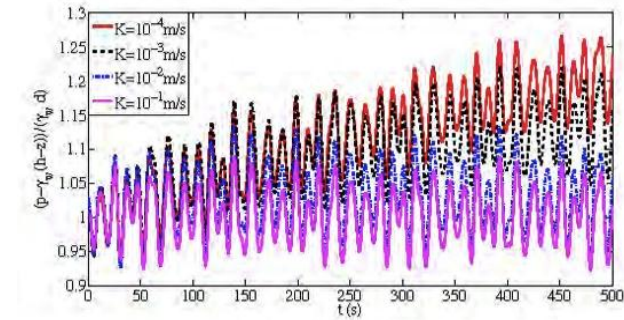


(c)  $\theta=225^\circ$

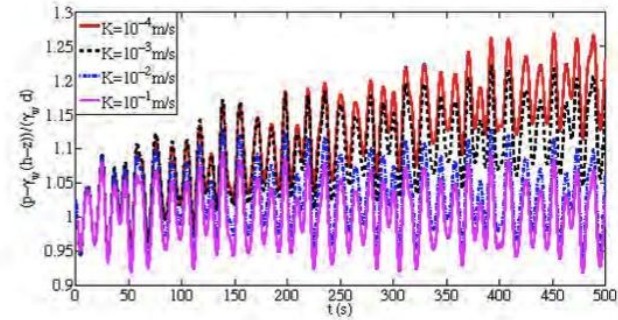


(d)  $\theta=315^\circ$

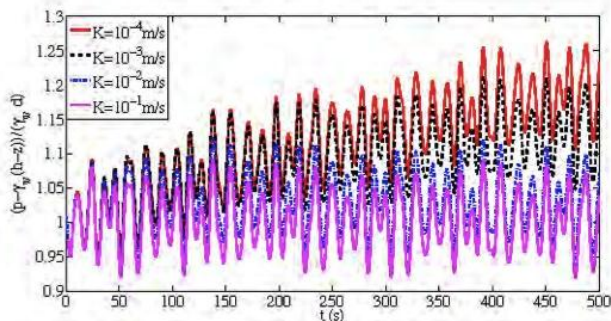
Figure 24 Normalised wave-induced pore pressure over time for various soil permeabilities ( $\kappa$ ) at different locations, with points based on  $\theta$  ( $z=10$  m,  $r/Lc=0.05$ )



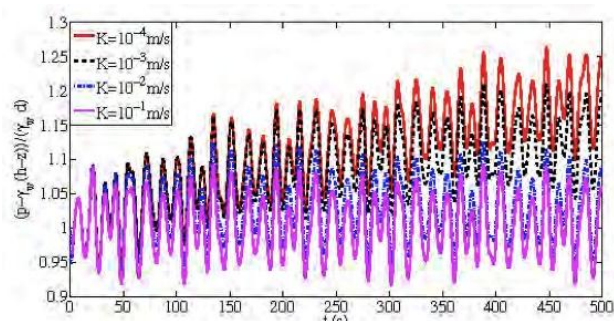
(a)  $r/L_c=0.05$



(b)  $r/L_c=0.1$



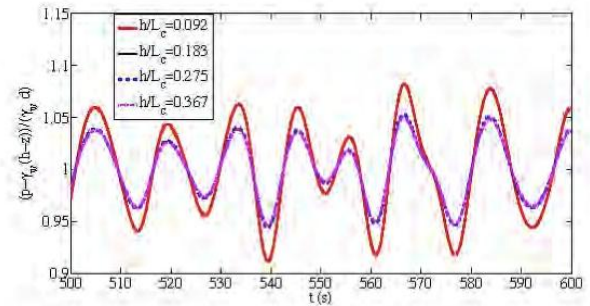
(c)  $r/L_c=0.2$



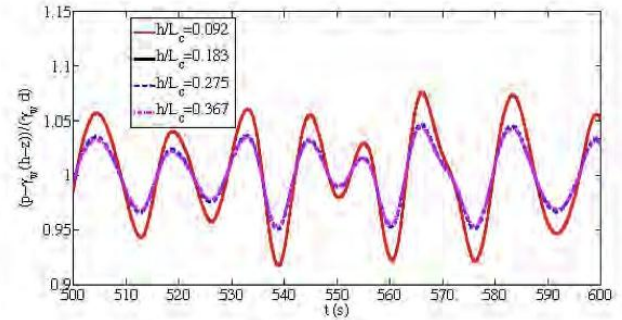
(d)  $r/L_c=0.5$

Figure 25 Normalised wave-induced pore pressure over time for various soil permeabilities ( $k$ ) at different locations, with points based on  $r$  ( $z=10$  m,  $\theta=135^\circ$ ).

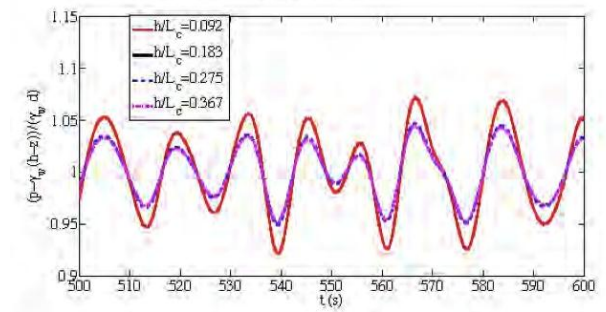
Four different seabed thicknesses were selected:  $h/L_c=0.092$ , 0.183, 0.275 and 0.367. Figure 26 and Figure 27 indicate a significant effect on the magnitude of the pore pressure when  $h$  is small. As  $h$  increased to a certain degree, the wave-induced pore



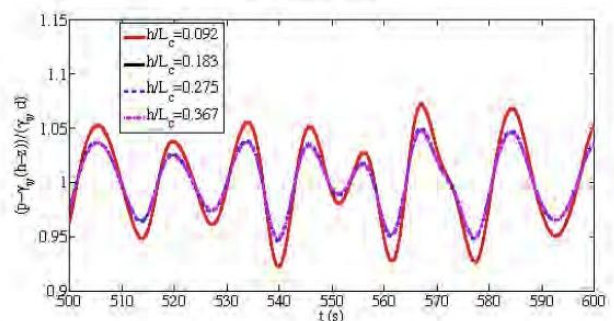
(a)  $\theta=45^\circ$



(b)  $\theta=135^\circ$



(c)  $\theta=225^\circ$



(d)  $\theta=315^\circ$

Figure 26 Normalised wave-induced pore pressure over time for various seabed thicknesses ( $h$ ) at different locations, with points based on  $\theta$  ( $z=10$  m,  $r/L_c=0.05$ )

pressures at different locations behaved independently of the seabed thickness. The possibility for and degree of liquefaction could be higher at higher amplitudes of pore pressure in seabeds with small thicknesses, which should be considered during the design of marine structures.

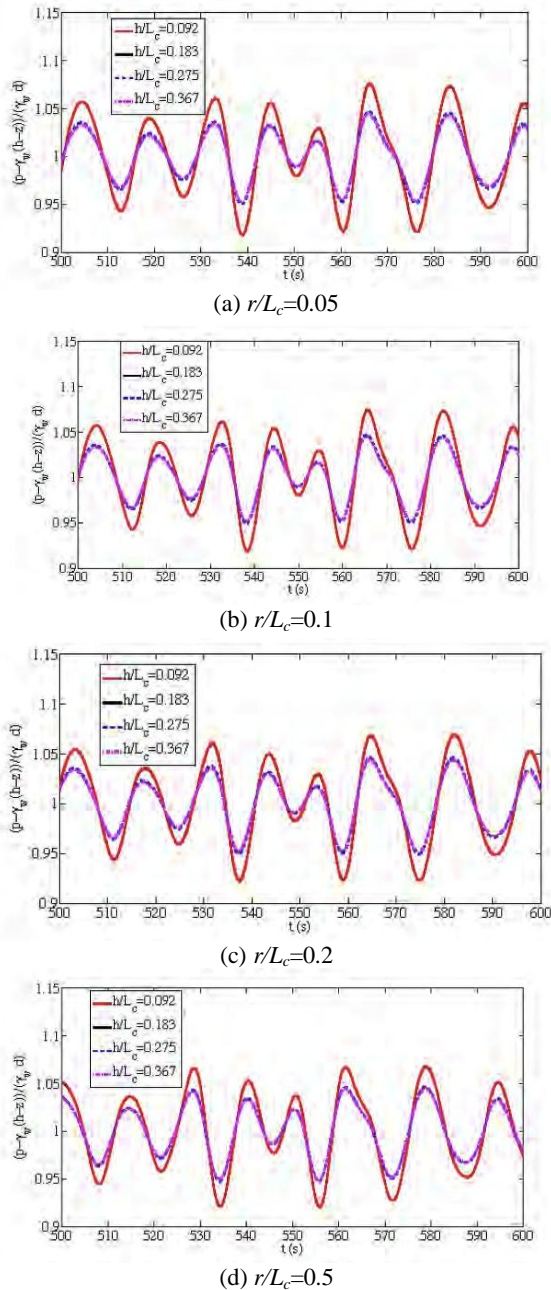


Figure 27 Normalised wave-induced pore pressure over time for various seabed thicknesses ( $h$ ) at different locations, with points based on  $r=10$  m,  $\theta=135^\circ$

#### 4. CONCLUSIONS

This paper describes a systematic and parametric investigation that was performed to study the wave-induced pore pressure around breakwater heads. The simulation was based on the DYNE3WAC program, which was capable of analysing both residual and oscillatory soil mechanisms simultaneously. The main soil model adopted for this study was the Pastor-Zienkiewicz Mark III model, which considers soil plasticity and has proved to be suited to wave and earthquake-induced soil responses. In general, both the wave and soil conditions could contribute to the potential liquefaction of seabeds, which has been demonstrated by both the previous work and the current thesis. This paper marks the first time random waves have been implemented to the analysis of wave-induced pore pressure. There may be some differences compared to the use of regular waves. The following conclusions can be drawn based on the results.

Both regular and random waves were applied for comparison, and the results showed that both types of waves brought about the accumulation and oscillatory variation of excess pore pressure. Because the regular waves possessed unique characteristics ( $T$ ,  $L$  and  $H$ ), the corresponding pore pressure fluctuates with a particular amplitude over time. However, an explicit residual trend was also observed over time. On the other hand, due to the irregularity of random waves, the oscillatory excess pore pressure fluctuated over time without a fixed amplitude. Therefore, it was possible that gentle random waves could introduce high amplitudes of excess pore pressure, thereby leading to liquefaction.

The wave characteristics were studied separately and indicated significant influences on pore pressure. Among these, the characteristic regular wave height ( $H_c$ ) played an important role in affecting both the build-up and oscillation of wave-induced pore pressure. Water depth directly affected the dynamic wave pressure on a seabed surface, thereby leading to major corresponding changes in excess pressure amplitudes. By affecting the frequency of the pore pressure variation, the rate of accumulation of pore pressure increased significantly as the characteristic regular wave period ( $T_c$ ) decreased.

A comparison has been made between the elastic model and the *PZ Mark III* elasto-plastic model, which indicated apparent differences in the simulation of both the amplitude and accumulation of pore pressure over time. The pore pressure showed faster accumulation, a higher equilibrium state and a greater amplitude in the elasto-plastic model.

Soil permeability was demonstrated to have the most significant effect on residual pore pressure. At low permeabilities, the excess pore pressure accumulated rapidly and reached a comparatively high equilibrium pore pressure. Hence, liquefaction was more likely to occur when the soil permeability was low.

The program used in this study, *DYNE3WAC*, proved some information about for studying the wave-induced pore pressure around breakwater heads. However, limitations still exist, which are summarised herein.

There are some shortcomings and limitations to the present model, such as when it simulates a large domain. The applied mesh should be as large as possible to decrease the space step inside each element, thereby improving accuracy. On the other hand, the enormous number of equations required for the number of elements demands a high consumption of computer memory (14.3 GB for 2304 elements). Therefore, it is possible to run cases only in a workstation. When the number of required equations is large enough, several *integer* type variables are also exceeded. Therefore, the number of elements is limited; for example, the maximum number of elements for the newly developed mesh cannot exceed 2304.

Although this number was sufficient to reach a state of convergence, it was not enough to refine the mesh in the vertical direction. However, the model was extremely sensitive to liquefaction depth. If the mesh was not fine enough, the distribution of liquefaction depths over the plane domain could not be obtained with reasonable accuracy (only up to approximately 0.25 m).

Another disadvantage identified in the *PZ Mark III* model was that when the mean effective stress was small, the stress path was inclined to cross the line into soil hardening, thereby leading to potential interruption of the program during calculation. A recommended solution is to treat a thin layer of the seabed on top as a *general elastic* model. Although this solution proved effective for solving the problem, the accuracy of the simulated results was influenced to some degree.

The *PZ* model doesn't consider the influence of the degree of rotation of principal stress axis induced in the seabed soil, which was included in Sassa and Sekiguchi (2001) model. Such an effects depends on the wave forms and therefore, the present study requires more advanced poro-elastoplastic model such as Sassa and Sekiguchi (2001).

## 5. REFERENCES

- Biot, M. A., (1956a) "Theory of propagation of elastic waves in a fluid-saturated porous solid, part I: low-frequency range", *J. Acoust. Soc. Am.* 28, pp168-180.
- Biot, M. A., (1956b) "Theory of propagation of elastic waves in a fluid-saturated porous solid, part II-higher frequency range". *J. Acoust. Soc. Am.* 28, pp181-190.
- Chan, A. H. C., (1995) "User Manual for DIANA-SWANDYNE II-Dynamic Interaction and Non-linear Analysis Swansea Dynamic Program Version II". School of Civil Engineering, University of Birmingham, UK.
- Goda, Y., (2000) "Random seas and design of marine structures". World Scientific, Singapore.
- Gökee, T., Sumer B. M. and Fredsøe, J., (1994) "Scour around the head of a vertical wall breakwater". International Conference on Hydro-Technical Engineering for Port and Harbor Construction, Yokosuka, Japan, pp1097-1116.
- Jeng, D.S., (1996) "Wave-induced liquefaction potential at the tip of a breakwater: an analytical solution". *Applied Ocean Research*, 18, Issues 5, pp229-241.
- Jeng, D.-S. (2013) *Porous Models for Wave-seabed Interactions*. Springer.
- Jeng, D.S. and Hsu, J.R.C., (1996) "Wave-induced soil response in a nearly saturated seabed of finite thickness". *Geotechnique*, 46, Issues 3:pp427-440.
- Jeng D-S & Ou J., (2010) "3D models for wave-induced pore pressure near breakwater heads". *Acta Mechanica*, 215, pp85-104.
- Li, J. and Jeng, D.S. (2008) "Response of a porous seabed around breakwater heads". *Ocean Engineering*, 35, Issues 8-9, pp864-886.
- Liu, H and Jeng D-S (2007) "A semi-analytical solution for random wave-induced soil response in marine sediments". *Ocean Engineering*, 34, Issue 8-9, pp1211-1224
- Mei C C and Foda M. A., (1981) "Wave-induced response in a fluid-filled poro-elastic solid with a free surface: A boundary layer theory". *Geophysical Journal of the Royal Astronomical Society*, 66, pp597-631.
- Okusa, S., (1985) "Wave-induced stress in unsaturated submarine sediments". *Geotechnique*, 35, Issues 4, pp517-532.
- Ou, J., (2009) Three-dimensional numerical modeling of interaction between soil and pore fluid. PhD thesis, University of Birmingham, UK.
- Pastor, M., Zienkiewicz, O.C. and Chan, A. H. C. (1990) "Generalized plasticity and the modelling of soil behavior". *International Journal for Numerical and Analytical Methods in Geomechanics*, 14, 151-190.
- Sassa, S and Sekiguchi, H. (2001) "Analysis of wave-induced liquefaction of sand beds". *Geotechnique*, 51, Issue 2, pp115-126.
- Sassa, S., Takayama, T., Mizutani, M. and Tsujio, D. (2006) "Field observations of the build-up and dissipation of residual pore pressures in seabed sands under the passage of storm waves". *Journal of Coastal Research, Special Issue 39*, 410-414.
- Smith, A.W. and Gordon, A.D. (1983) "Large breakwater toe failures". *Journal of Waterway, Port, Coastal and Ocean Engineering*, 109, pp253-255.
- Stoker, J. J. (1957) "Water waves". Interscience Publishers, Inc., New York.
- Sumer, B.M. and Fredsøe, J., (2002) "The mechanics of scour in the marine environment". World Scientific, Singapore.
- Vun, P. L. (2005) *Experimental and Numerical Studies on Wave-induced Liquefaction to Soils around Marine Structures Funded in the Seabed*. Ph.D. Thesis, University of Birmingham.
- Wood, W. L., (1990) *Practical Time-stepping Scheme*, Clarendon Press, Oxford.
- Xu, H. X. and Dong, P. (2011) "A probabilistic analysis of random wave-induced liquefaction". *Ocean Engineering*, 38, Issue 7, pp860-867.
- Yamamoto, T., Koning, H., Sellmeijer, H., and Van Hijum, E., (1978) "On the response of a poroelastic bed to water waves". *Journal of Fluid Mechanics*, 87, pp193-206.
- Ye J and Jeng D-S (2012) "Response of seabed to natural loading-waves and currents". *Journal of Engineering Mechanics, ASCE*, 138(6), 601-613.
- Zienkiewicz, O.C., Chan, A.H.C., Pastor, M., Schrefler, B.A., Shiomi, T., (1999) *Computational Geomechanics with special reference to Earthquake Engineering*. Wiley, Chichester.